Available online at www.sciencedirect.com
ScienceDirect
Continental Shelf Research 28 (2008) 318–337
CONTINENTAL SHELF RESEARCH
www.elsevier.com/locate/csr

Tides and mixing in the northwestern East China Sea Part I: Rotating and reversing tidal flows

Iossif Lozovatsky[b,c,*], Zhiyu Liu[a], Hao Wei[a], H.J.S. Fernando[b]

[a]*Physical Oceanography Laboratory, Ocean University of China, Qingdao 266100, PR China*
[b]*Environmental Fluid Dynamics Program, Department of Mechanical and Aerospace Engineering, Arizona State University, AZ 85287-8909, USA*
[c]*P.P. Shirshov Institute of Oceanology, Russian Academy of Sciences, Moscow 117997, Russia*

Available online 14 September 2007

Abstract

Bottom-mounted ADV and ADCP instruments in combination with CTD profiling measurements taken along the Chinese coast of the East China Sea were used to study the vertical structure of temperature, salinity, and velocity in reversing tidal currents on a shallow inner shelf and in rotating tidal flows over a deeper sloping bottom of the outer shelf. These two regimes of barotropic tide affect small-scale dynamics in the lower part of the water column differently. The reversing flow was superimposed by seiches of ~2.3 h period generated in semienclosed Jiaozhou Bay located nearby. As the tidal vector rotates over the sloping bottom, the height of the near-bottom logarithmic layer is subjected to tidal-induced variations. A maximum of horizontal velocity U_{max} appears at the upper boundary of the log layer during the first half of the current vector rotation from the minor to the major axis of tidal ellipse. In rotating tidal flow, vertical shear generated at the seafloor, propagated slowly to the water interior up to the height of U_{max}, with a phase speed of ~5 m/h. The time-shifted shear inside the water column, relative to the shear at the bottom, was associated with periodically changing increases and decreases of the tidal velocity above the log layer toward the sea surface. In reversing flows, the shear generated near the bottom and the shear at the upper levels were almost in phase.

Keywords: Tidal currents; East China Sea; Seiches; Shear; Convection; Internal waves

1. Introduction

The northern part of the East China Sea (ECS), which is also called the Yellow Sea (YS), is a shallow semi enclosed basin, bounded by the China coast from the west and the Korean peninsula from the east (Fig. 1). A shallow basin, the Bohai Sea (BS), is in the northwestern corner of YS. The central part of YS is several hundred kilometers to the north and northwest from the ocean shelf break. A trough of about 90 m in depth stretches along the south–north axis of the basin. The sloping shelf along the China coast is relatively shallow and gentle, while the Korean shelf deepens rather sharply into the trough.

A sketch of the current system in ECS and adjacent seas is given in Fig. 2. It is based on Su (1998), showing that in the wintertime the main branch of the Kuroshio enters ECS southeast of Taiwan. Then the current flows to the northeast along the continental slope and exits ECS south of the Kyushu Island through the Tokara Strait. The speed of this flow usually exceeds 0.4 m/s (Song, 1994). The Tsushima Warm Current splits from the main branch of the Kuroshio approximately 200 km west of the Kyushu Island, entering ECS as a northward flow with the maximum speed of 0.25 m/s (Song, 1994). This flow exits ECS through the Tsushima Strait. The Taiwan Warm Current, which enters ECS from the Taiwan Strait, is weak in wintertime, not exceeding 0.13 m/s (Yuan and Su, 1984). The Yellow Sea Warm Current (YSWC) with a maximum speed of about 0.25 m/s flows northward through YS central trough (Fairbridge, 1966). The current, which directly affects our mooring locations, is the Yellow Sea Coastal Current. This cold current flows southward along

*Corresponding author. Environmental Fluid Dynamics Program, Department of Mechanical and Aerospace Engineering, Arizona State University, AZ 85287-8909, USA.
E-mail address: i.lozovatsky@asu.edu (I. Lozovatsky).

0278-4343/$ - see front matter © 2007 Elsevier Ltd. All rights reserved.
doi:10.1016/j.csr.2007.08.006

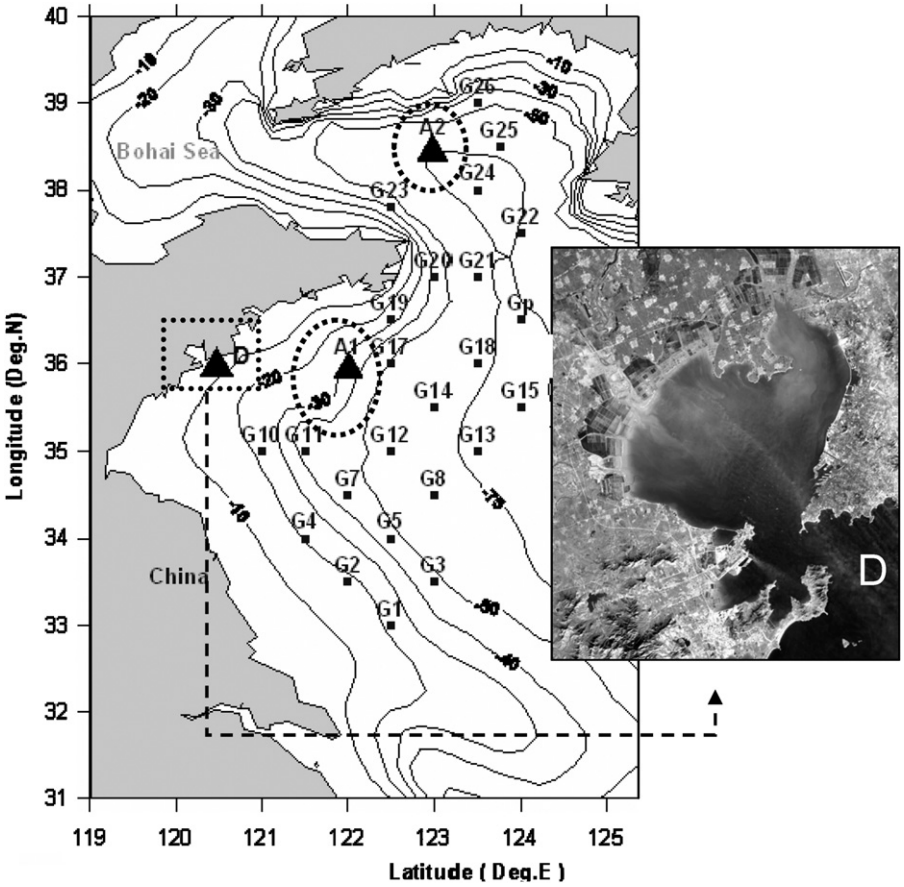

Fig. 1. Locations of mooring stations A1, A2 (March 2005), and **D** (December 2005) in the northwestern East China Sea. The region surrounding St. D is enlarged in the insertion showing the Jiaozhou Bay of the China coast. St. D was set up about 2 km to the east from the mouth of the bay and 1.2 km to the south from the northern coastline. CTD stations of the hydrographic survey taken in March 2005 are marked as G1,…,G25 in the background of bottom topography.

the China coast all year around, dominating the circulation on the northwestern shelf of Yellow Sea.

In this paper, we focus on the tidal dynamics of shallow waters in the northwestern sector of ECS. To this end, ADV and ADCP data obtained in 2005 by oceanographers of Ocean University of China will be employed, including three bottom-mounted stations in the coastal zone of China and a polygon-style series of CTD profiling measurements (see Fig. 1). A description of the observational setup and basic meteorological conditions during the measurements are given in Sections 2 and 3, respectively, followed by an analysis of currents at mooring sites by applying a tidal model of six major constituents (Fang 1974, 1976, 1981) for the northern part of ECS (Section 4). In the same section, the interaction of tides with local seiche oscillations is addressed. The thermohaline structures at all stations and internal waves at one of the stations are discussed in Section 5. Of particular interest is the evolution of vertical velocity profiles and associated vertical shear, which are analyzed in Section 6. Section 7 summarizes the results. Analysis of the near-bottom turbulence in the region is given in Lozovatsky et al. (2007).

2. Observations

The data analyzed in this study were collected in March and December of 2005 in the northwestern part of ECS during two cruises of R/V Dongfanghong-2 of Ocean University of China. The mooring measurements were taken at three bottom-mounted stations at different times; St. A1 (March 26–27, 35.90°N, 121.58°E, the mean water depth $z_B = 38$ m), St. A2 (March 20–21, 38.50°N, 123.00°E, $z_B = 58$ m), and St. D (December 14, 36.04°N, 120.32°E, $z_B = 19$ m). Bottom topography in the region and the locations of the mooring stations are shown in Fig. 1. The Station D was near the coastline (~1.2 km from the shore), only 2 km away from the mouth of the Jiaozhou Bay (JB). Station A1 was located almost at the same latitude as St. D, but 115 km to the east. The closest distance from St. A1 to the coastline in the northwestern direction across the isobaths is 90 km. Station A2 was set up in a deeper basin ($z_B = 56$ m) of YS. A hydrographic survey of 22 CTD stations was taken between March 19 and March 26, 2005.

The moorings were equipped with a 6 MHz Nortek "Vector" ADV and a 600 kHz RDI 4-beam Jenus ADCP.

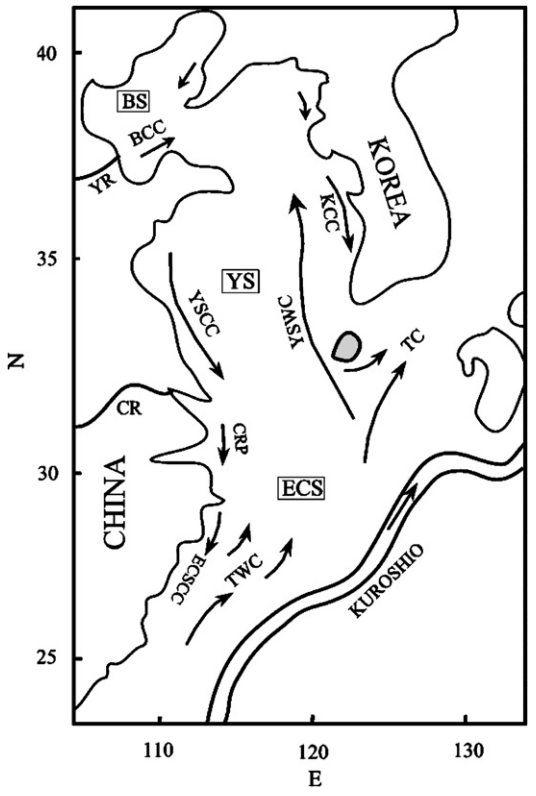

Fig. 2. Major currents in the East China Sea [ECS], and adjacent waters (Yellow Sea [YS] and Bohai Sea [BS]) in wintertime: TWC—Taiwan Warm Current, TC—Tsushima Current, YSWC—Yellow Sea Warm Current; YSCC—Yellow Sea Coastal Current; KCC—Korean Coastal Current; BCC—Bohai Coastal Current, CRP—Changjiang River Plume, ECSCC—East China Sea Coastal Current; CR and YR are Changjiang and Yellow Rivers, respectively. The figure is based on Su (1998).

Both instruments delivered components of current velocity during 25 h (over two semidiurnal tidal cycles) at each station. At Stations A1 and A2, the height of the upward-looking ADV sampling volume was set up at 0.95 m above the bottom (0.95 mab) with the instrument at 0.8 mab. The sampling rate was 64 Hz, with data recorded over 32 s (2048 samples of each variable) with 10 min interval between the bursts. At St. D, the ADV was looking downward and the height of its sampling volume was at 0.45 mab with the instrument located at 0.6 mab because of a modified supporting frame. The sampling rate was reduced to 16 Hz but the data were recorded continuously during the observational period.

The ADCP profiles of $u(\zeta)$, $v(\zeta)$, and $w(\zeta)$, where ζ is the height above the seafloor, were obtained with a vertical resolution of 0.75 m through the whole water column at Sts. A1 and D, but only up to 38 mab at St. A2. (At this mooring, the data quality assessment only allowed the first 48 cells of the ADCP data). The along-beam velocities were measured with a ping rate of 2 Hz; the data were ensemble averaged over 2 s (i.e., four pings) before being recorded in earth coordinates. The variations of the sea surface elevation were assessed through the pressure measurements using the ADCP pressure sensor. The first level of ADCP measurements was at a height of 2.4 mab at Sts. A1 and A2 and at $\zeta = 2.8$ mab at St. D. The data recording method was the same as for ADV: a 10-min burst cycle at A1 and A2 and continuous at St. D.

During 25 h of ADCP and ADV measurements at each site, 50 CTD profiles were taken at St. D (every 30 min) but only 13 profiles were obtained at A1 and A2 (every 2 h). The Campbell Scientific Datalogger CR1000 was used for standard atmospheric measurements onboard. Wind speed and wind direction were measured by RM YOUNG wind monitor 05106-10 (http://www.campbellsci.ca/Catalogue/05106-10.html). The Campbell Scientific HMP45C-L probe was used for the measurements of air temperature and relative humidity (http://www.campbellsci.com/hmp45c-l).

3. Wind forcing and surface fluxes

The measurements at Sts. A1 and A2 were taken in late March under calm and moderate winds. At A1, the wind speed at 10 m above the surface was $\langle W_{10} \rangle = 4.0 \pm 1.8$ m/s and at A2, $\langle W_{10} \rangle = 5.2 \pm 2.6$ m/s ($\langle\ \rangle$ indicates the mean $\pm$ the standard deviations). Wind forcing at A1 had two distinguished periods (see Fig. 3(a)). During the first 9 h of observations (March 26, 15:00–March 27, 00:00), the speed of the almost southerly wind (the wind direction $\langle \Theta \rangle = 168^\circ \pm 7.5^\circ$) was $\langle W_{10} \rangle = 6.0 \pm 0.54$ m/s. The corresponding variations of friction velocity at the sea surface $u_{*(ss)} = \sqrt{|\bar{\tau}_a|/\rho_w}$, where $|\bar{\tau}_a|$ is the magnitude of wind stress and ρ_w the water density, are shown in Fig. 3(b). At St. A1, during the first 9 h of measurements, the mean wind stress $\langle|\bar{\tau}_a|\rangle$ was 5×10^{-2} N/m^2 with $rms(|\bar{\tau}_a|) = 9 \times 10^{-3}$ N/m^2; the wind work was $\langle E_{10} \rangle = 0.3 \pm 0.08$ W/m^2, where $E_{10} = W_{10}|\bar{\tau}_a|$. After midnight of March 27, the wind speed decreased below 2 m/s at 01:30 (see Fig 3(a)), and then W_{10} weakly fluctuated between 2 and 4 m/s (the corresponding $\langle|\bar{\tau}_a|\rangle = 9 \times 10^{-3}$ N/m^2, and $\langle E_{10} \rangle = 0.02$ W/m^2) until the end of observations.

At St. A2, where mooring measurements started on March 20, 2005 at the same time of the day as at A1 (15:00 local time; LT thereafter in all figures) the wind varied between 2 and 6 m/s during the first 10 h of observations. After midnight of March 21, a continuous increase of the wind speed was observed from 1 m/s at 2:00 to 9.1 m/s around noon (Fig. 3(a)). Then the wind gradually decreased to ~7 m/s at the end of the observational period. The corresponding $|\bar{\tau}_a|$ at A2 ranged between 3.5×10^{-3} and 1.2×10^{-1} N/m^2 ($\langle u_{*(ss)} \rangle = 6.2 \times 10^{-3}$ m/s, see Fig. 3(b)) and the wind work E_{10} changed from ~0.04 to 1.1 W/m^2.

At both stations A1 and A2, the difference between the air and sea surface temperatures $\Delta T = T_a - T_w$ varied in a narrow range: $\pm 1.5\,^\circ$C (Fig. 3(c)). At A1, the highest daytime air temperature T_{ad} was 5.9 °C and the lowest nighttime temperature $T_{an} = 2.5\,^\circ$C. The sea surface temperature T_w ranged between 3.65 °C at night and 4.25 °C in the afternoon. At A2, the air temperature was in the range $T_a = 5.1$–$3.4\,^\circ$C, while T_w decreased from 4.25

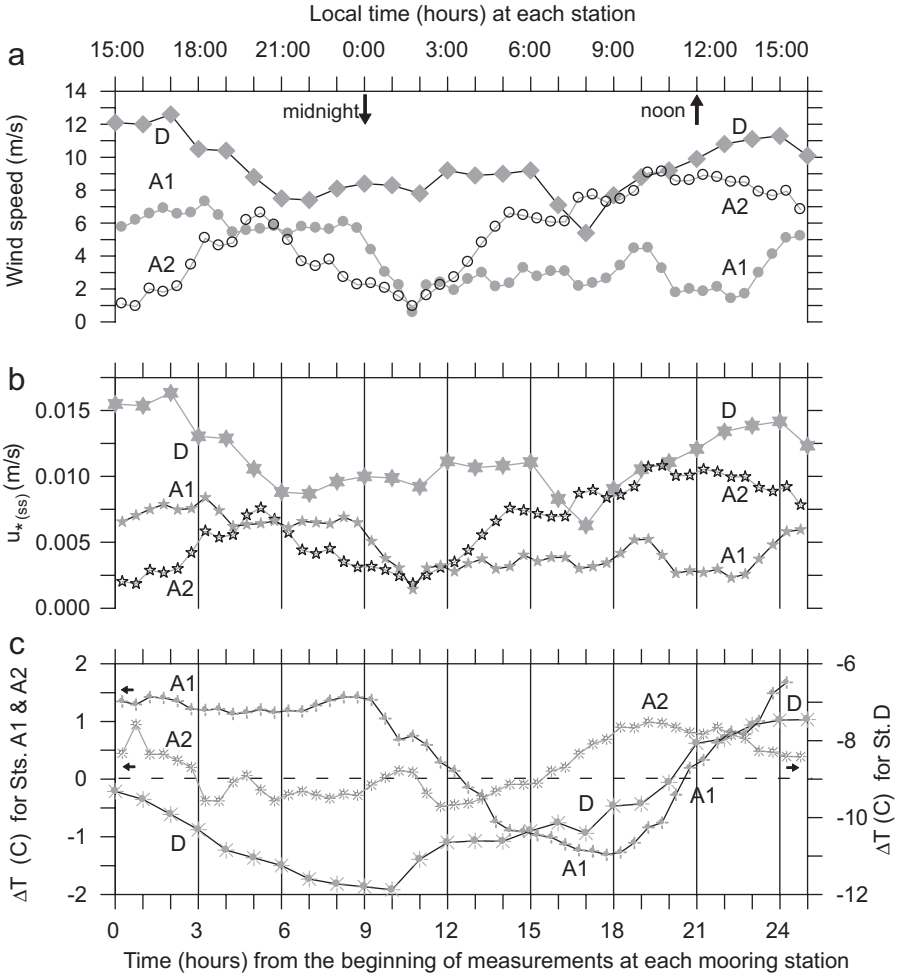

Fig. 3. Wind speed (a), friction velocity at the sea surface (b), and the difference ΔT between the air T_a and sea surface T_w temperatures (c) at St. A1 (March 26–27, 2005), St. A2 (March, 20–21), and St. D (December 14–15, 2005). The measurement cycles started at 15:00 local time (LT) at all stations.

to 3.8 °C during the first 11 h of measurements, remaining almost constant $\langle T_w \rangle = 3.82\,^{\circ}\mathrm{C}$ thereafter. The corresponding heat and buoyancy fluxes at the see surface (not shown here) changed sign during the observational period, albeit were weak and thus did not affect the water interior below the surface layer.

Contrary to the measurements carried out at Sts. A1 and A2 in March of 2005, the measurements taken at St. D in December 2005 were strongly influenced by surface convective flux. After midnight of December 15, T_a was 12 °C below T_w and the difference ΔT still remained highly negative into the next afternoon ($\Delta T = -7.4\,^{\circ}\mathrm{C}$) leading to a strong convection-favorable buoyancy flux with the median of $\sim 1.3 \times 10^{-7}$ W/kg. This, as shown in Lozovatsky et al. (2007), is comparable with the dissipation of turbulent kinetic energy generated by the ebb tide in bottom boundary layer (BBL). The wind forcing at St. D was relatively stable during the whole 25-h period of observations; the speed of the northwestern wind was $\langle W_a \rangle = 9.3 \pm 1.7$ m/s. The mean friction velocity $\langle u_{*(ss)} \rangle = 1.1 \times 10^{-2}$ m/s (Fig. 3), which is a characteristic $u_{*(ss)}$ for a mild storm, producing the energy flux of 1.37 W/m^2 on the average. Note that all components of the net heat flux J_q and the corresponding buoyancy flux J_b as well as the wind stress $|\bar{\tau}_a|$ were computed using the bulk formula of Matlab air–sea interaction toolbox (http://sea-mat.whoi.edu) based on 30-min averaged standard meteorological data.

4. Tidal and sub-tidal currents

In the absence of typhoons, which sometimes affect the ECS in late summer/early autumn, tidal currents produced by barotropic and baroclinic tides are the most powerful dynamic component nearly in all regions of the sea. The barotropic tide is predominantly semidiurnal M_2 (the tidal frequency $\omega_{td} = 1.41 \times 10^{-4}\,\mathrm{s}^{-1}$), but five other tidal constituents (O_1, K_1, S_2, M_4, and MS_4) are also important for the assessment of the tidal influence on currents and sea surface elevation. In the central basin of the northern ECS, the tidal flow exhibits almost circular rotation (Lee and Jung, 1999; Kang et al., 2002), while closer to the coasts,

tidal ellipses are more stretched across the topography. In some areas, rotating vector of tidal current transforms to a reversible flow dominated by one horizontal component. Our three testing sites are representative for three different regimes of the barotropic tide in ECS. These are the regular, slightly stretched ellipse of counter-clockwise rotating flow (St. A1); the irregular, twisted ellipse at St. A2; and a reversible flow at St. D, which, in turn, was affected by local currents presumably of seiche origin due to its closeness to JB. Figs. 4(a)–6(a) illustrate the differences between tidal flows at the ADCP/ADV locations showing the hodographs of 1-h averaged current vectors during two semidiurnal cycles. Because the shape of every hodograph transforms very little with depth, only one or two examples for each station are shown. Profiles of the amplitude of M_2 tidal constituent $U_{M2}(\zeta)$ and tidal residuals $U_{rs}(\zeta)$ for Sts. A1 and A2 are shown in Figs. 4(b) and 5(b). The amplitude of the M_2 constituent, away from the surface and BBL, is 0.35 m/s at A1 and 0.42 m/s at A2 with characteristic magnitudes of tidal residuals $U_{rs}\sim 0.5$ and $U_{rs}<2$ cm/s, respectively. Time variations of horizontal velocity components u and v (each sample is 1-min averaged ADCP data over 10-min burst period) agree nearly perfectly with the tidal model of Fang (1974, 1976, 1981) containing six major constituents (see Figs. 4(c) and 5(c)), which accounts for more than 98% of the total

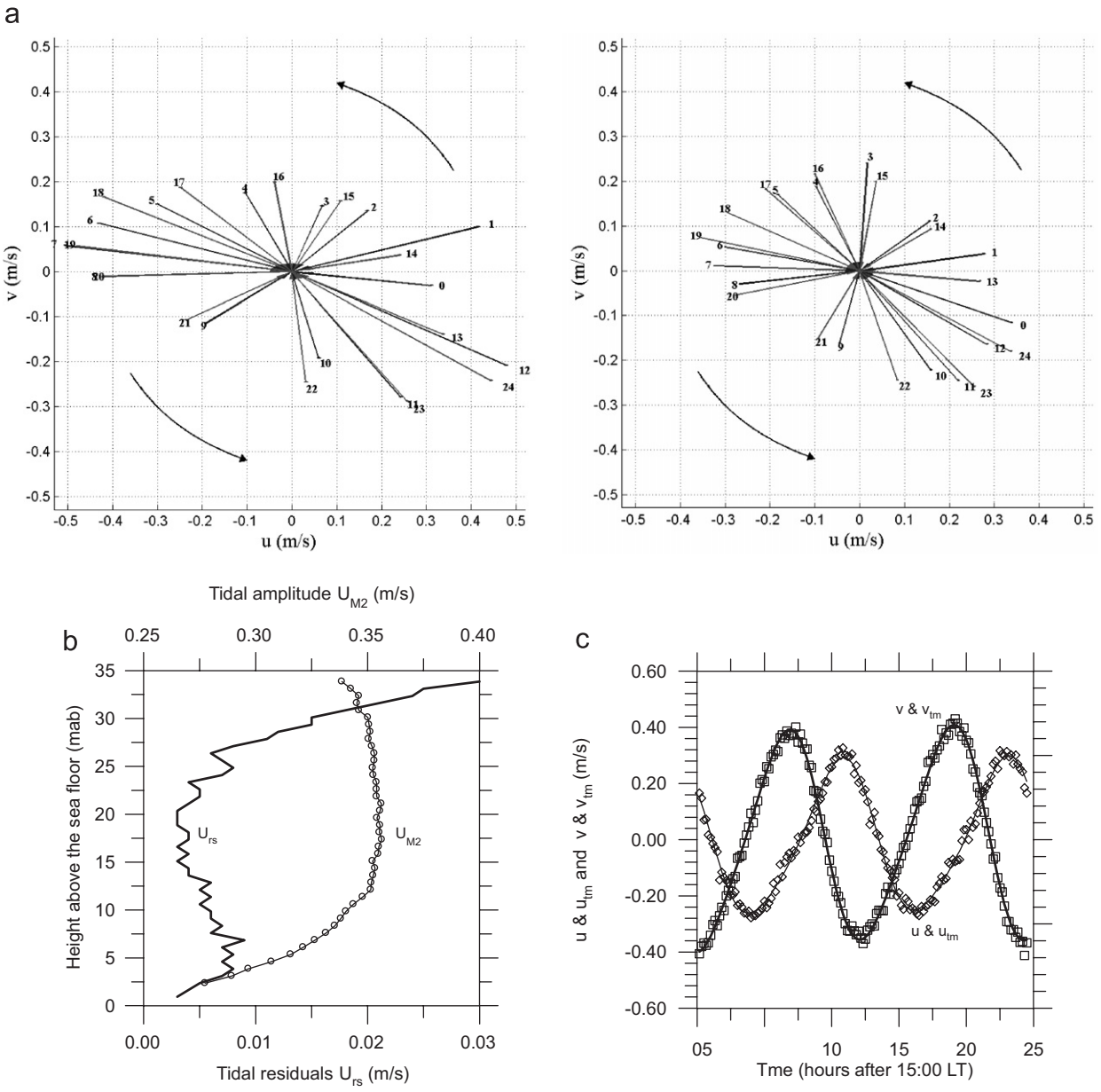

Fig. 4. St. A1: (a)—Hodographs of rotating tidal flow at $\bar{z}\approx 35.5$ m ($\zeta=2.36$ mab, ADCP cell 1, left) and $\bar{z}\approx 4$ m ($\zeta=33.86$ mab, ADCP cell 44, right) for two M_2 tidal cycles; the numbers at the arrows are times of 1-h averaged current vectors after 15:00 of March 26, 2005. (b)—Vertical profiles U_{M2} of the amplitude of M_2 barotropic tide averaged over two semidiurnal cycles and the corresponding tidal residuals U_{rs}. (c)—Approximation of the ADCP components u and v by a sum of 6 major tidal constituents (u_{tm} and v_{tm}) using the model of Fang. The example is given for $\zeta=7.6$ mab ($\bar{z}\approx 30$ m).

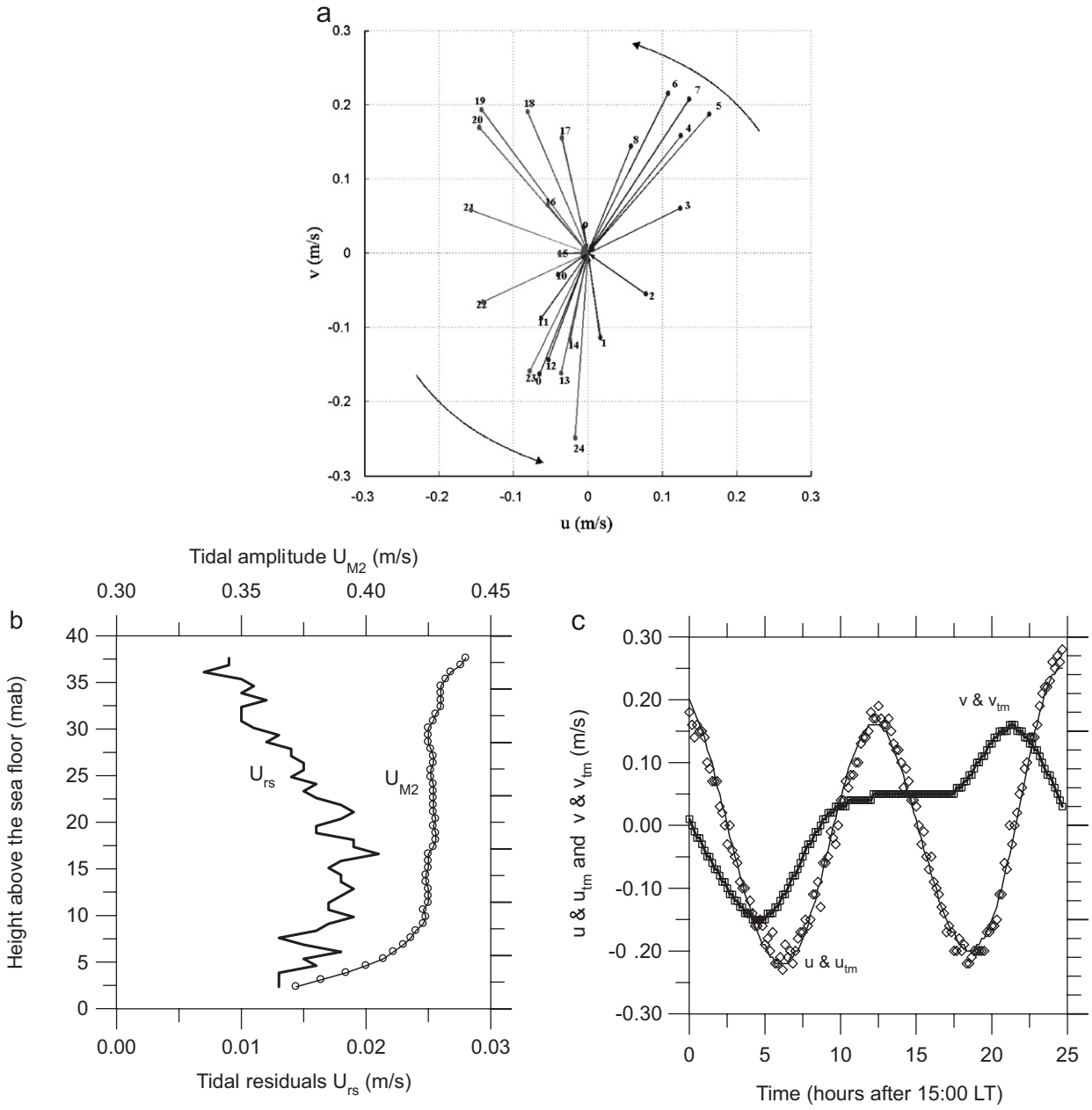

Fig. 5. St. A2: (a)-Hodograph of rotated flow at $\bar{z} \approx 35.5$ m ($\zeta = 18.1$ mab, ADCP cell 22) for two tidal cycles of M_2; the numbers at the arrows are times of 1-h averaged current vectors after 15:00 of March 20, 2005 (see the numbers). (b)—Vertical profiles U_{M2} of the amplitude of M_2 barotropic tide averaged over two semidiurnal cycles and the corresponding tidal residuals U_{rs}. (c)—Approximation of the ADCP components u and v by a sum of 6 major tidal constituents (u_{tm} and v_{tm}). The example is given for $\zeta = 20$ mab ($\bar{z} \approx 37$ m).

variance of the observed currents. This signifies complete dominance of the barotropic tidal flow in the regions at time scales larger than 10 min.

The flow dynamics were quite different near the coast at the shallow St. D, where the variation of sea surface elevation was totally governed by barotropic tide (Fig. 6(b)), but currents (Fig. 6(c)) were only partly dependent on the tidal forcing. The amplitude of the cross-shelf, meridional component v was less than 0.05 m/s and fluctuations of $v(t)$ were not of tidal origin. The alongshore, zonal component $u(t)$ was much higher. The amplitude of the westward flood current (~0.4 m/s) was approximately twice that of the eastward current during the ebb phase. The residuals between the observed reversible, non-symmetrical zonal flow $u(t)$ and its approximation by the tidal model of Fang revealed an oscillatory zonal flow with non-stationary period (see Fig. 6(c)). During the ebb phase, the amplitude of these oscillations was comparable, or even higher, than the tidal amplitude of zonal velocity.

To evaluate characteristics and possible origin of higher-frequency flow observed at St. D, we computed spectra of tidal residuals of the velocity magnitude U_{rs} (at $\zeta = 0.45$ mab) and residuals of the sea surface elevation η_{rz}. Note that spectral density $E_U(f)$ is a combination of u_{rs} and

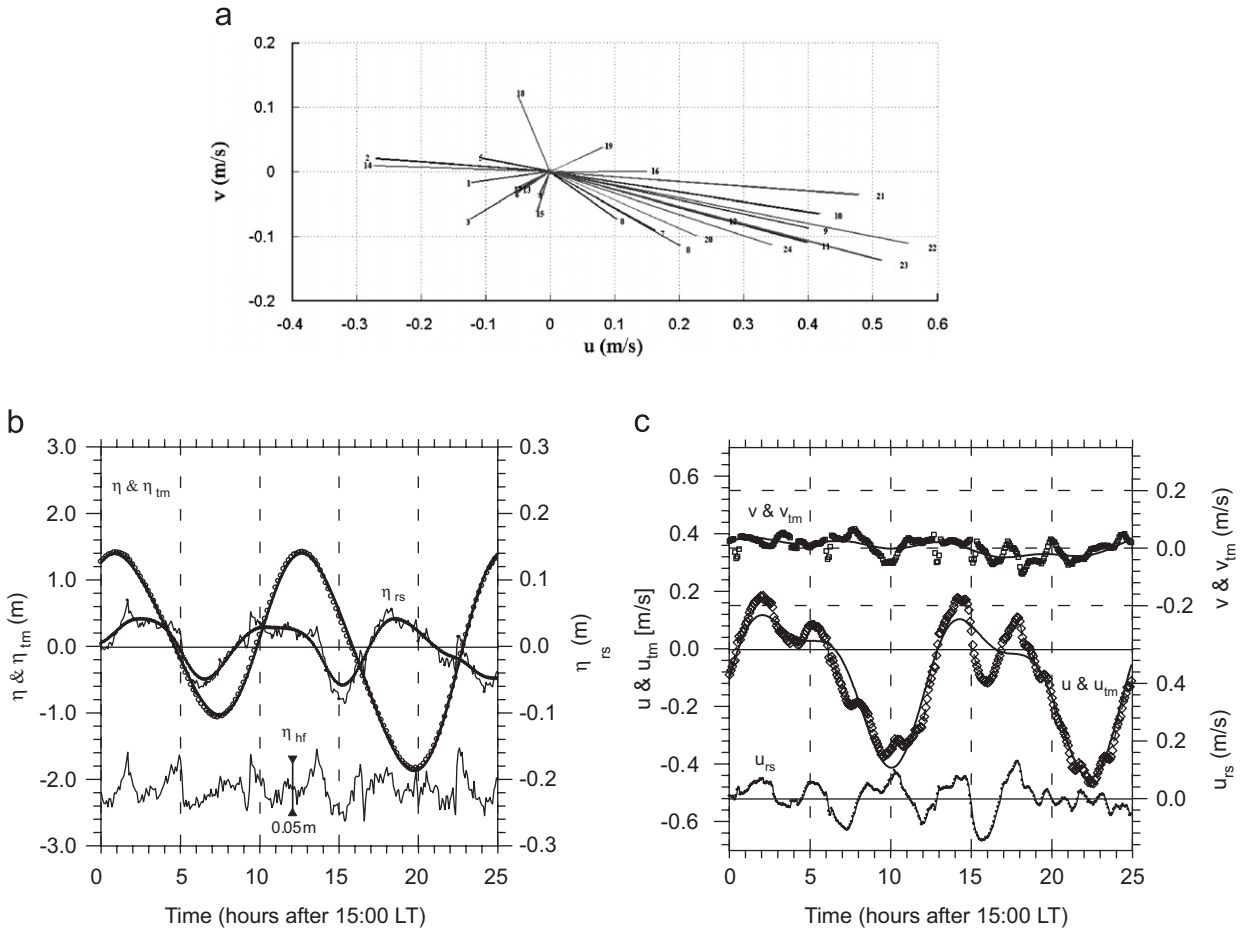

Fig. 6. St. D: (a)—Hodograph of almost reversible tidal flow at $\bar{z} \approx 13$ m ($\zeta = 5.8$ mab, ADCP cell 5) for two M_2 tidal cycles; the numbers at the arrows are times of 1-h averaged current vectors after 15:00 of December 14, 2005. (b)—Measured sea surface elevation η that is well matched by a tidal model η_m with 6 major tidal constituents. Tidal residuals η_{rz} are shown with a low-frequency trend, which being subtracted from η_{rz} gives the high-frequency component η_{hf} that is shown at the bottom of the figure with its individual vertical scale. (c)—ADV current components u and v at $\zeta = 0.45$ mab ($\bar{z} \approx 18.5$ m) and their approximations u_m and v_m by tidal regional model. The corresponding record of tidal residuals u_{rs} is a superposition of tidal and non-tidal velocity oscillations.

v_{rs} spectral components: $E_U = 0.5(E_{urs} + E_{vrs})$. The ADV data used for the spectral analysis were low-pass filtered and "burst resampled" to reduce the effective sampling rate by averaging $u_{rs}(t)$ and $v_{rs}(t)$ at 1-min segments with a 5-min time step between the segments. This eliminates high frequency fluctuations in the initial records, which can be considered as a noise for the analysis of low-frequency fluctuations. The same procedure was applied to the initial record of η_{rz}. The variance preserving spectra $fE_U(f)$ and $fE_{sse}(f)$, where $E_{sse}(f)$ is a spectral density of the sea surface elevation, are shown in Fig. 7 at a semi log scale to emphasize the contribution of specific frequency bands to the total variances $\overline{U_{rs}^2}$ and $\overline{\eta_{rs}^2}$. The frequency of the salient maximum f_o in both spectra appears to be almost identical corresponding to the period of oscillation $t_o = 1/f_o \approx 2.3$ h. The oscillations with frequencies lower than f_o were almost completely suppressed by subtracting the tidal trend from initial records and by high-pass filtering with a cut-off frequency of $0.04f_N$ (using the 2nd order Butterworth filter); $f_N = 1/2\Delta t$ the Nyquist frequency. The spectra shown in Fig. 7 also exhibit statistically confident maxima at the sub-harmonic frequencies f_o/n ($n = 1, 2, 3, \ldots$). The periods of several odd sub-harmonics are marked in Fig. 7 by arrows; most even sub-harmonics are also evident.

The origin of $t_o = 2.3$ h oscillations can be related to the seiche generation in JB and its interaction with the barotropic tide at the exit of the bay. Because the bay is not an enclosed basin and open to a larger sea (see Fig. 1), the seiche period can be estimated using a modified Merian formula, $\tau_{sch} = 4L_{JB}/c_{sch}$ (i.e., Knauss, 2000), where the seiche phase speed $c_{sch} = (gH_{JB})^{1/2}$ and a characteristic depth and width of JB are H_{JB} and L_{JB}, respectively. Taking the longest distance between the northern shore and the bay mouth, which is $L_{JB} = 18$ km, as a characteristic diameter of the main body of JB and the mean depth $H_{JB} = 7$ m (Liu et al., 2004), we obtain an estimate of $\tau_{sch} = 2.4$ h. This estimate matches well with the dominant observed periods evident from Fig. 7. The result suggests that the flow at St. D is governed by a superposition of tidal constituents (still having the M_2 tide as the major

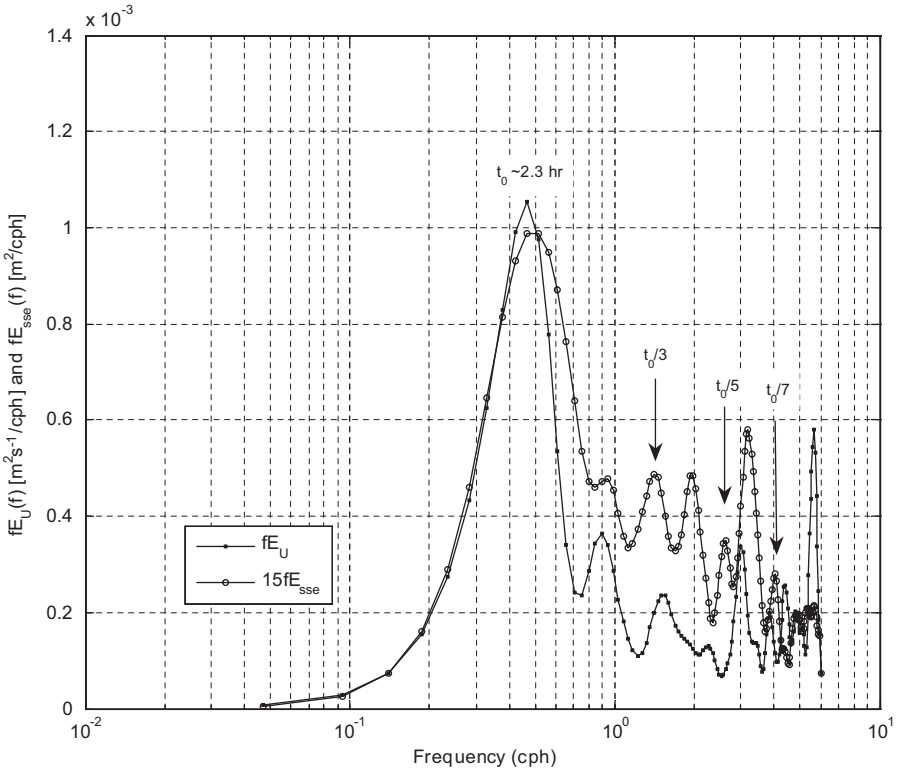

Fig. 7. Energy-preserving frequency spectra of tidal residuals of the velocity magnitude $fE_U(f)$ and the sea surface elevation $fE_{sse}(f)$. To facilitate depiction of the spectra on the same vertical scale, the sea surface spectrum was multiplied by a factor of 15. The main maximum (t_o~2.3 h) and its odd sub-harmonics t_o/n, where $n = 1, 3, 5, \ldots$, are pointed by arrows.

contributor) and a number of seiche harmonics. Seiches dominated the flow during the ebb tide because of the relatively small tidal velocity in this phase. Note that a simple seiche model of a constant-depth open channel allows only odd sub-harmonics, $n = 1, 3, 5, \ldots$, but the sea surface data and to a lesser extent the velocity measurements contain all sub-harmonics of f_o from 2 to at least 7. An explanation can be offered considering time variations of the direction of the wind. At the beginning of the observational period, the wind direction was 330°, i.e. exactly towards the open end of the bay (see Fig. 1) and the wind speed varied between 10 and 12 m/s. In the next 15 h, the wind gradually ceased to 6–8 m/s, turning to the west. The westerly wind can produce a regular close-basin seiche with a period $\tau_{sch} = 2L_{WE}/c_{sch} \approx 70$ min, where the west-east diameter $L_{WE} \approx 15$ km. The frequency of this wave is about twice of f_o, and therefore the perceived even harmonics of f_o may actually represent a close-basin seiche and its sub-harmonics, which interferes with the open-basin seiche.

5. Vertical thermohaline structure and internal waves

Stratification in ECS in early spring (Sts. A1 and A2) and early winter (St. D) is generally weak. Often seasonal storms and winter cooling at the sea surface mix the water column down to the bottom, but constant river discharge and precipitations quickly restore weak stable stratification, particularly in deeper basins. Cooler and fresher waters are located along the coast of China with increasing temperature, salinity, and density toward the central basin. An example of spatial distribution of T, S, and σ_θ in late March 2005 is given in Fig. 8 based on the hydrographic survey taken in the area. The spatial distribution of thermohaline characteristics in Fig. 8 generally follows climatological variations of regional water masses. Yellow Sea Warm Water (T~8 °C) is to the south and east from St. A1; Yellow Sea Coastal Cold Water (T~2 °C) is to the north. Apparent tidal variations of the near bottom temperature at St. A1 (see Figs. 9 and 10(a)) are caused by the advection of tidal flow across the horizontal temperature gradient at the sloping shelf. Temperatures at $\zeta = 5$, 10, and 15 mab, obtained from sparse CTD profiles closely follow the near-bottom temperature at $\zeta = 0.95$ (Fig. 9), showing $\Delta T = 0.09$ °C as the largest difference between $T_{0.95}$ and T_{15}. This suggests that the observed semidiurnal range of temperature variations at $\zeta = 0.95$ mab, $\delta T_{0.95} = 0.16$ °C, cannot be attributed to vertical displacements caused by internal tide in the region. In the deeper northern basin around St. A2 (Fig. 10(b)), the temperature of the lower 20–25 m of the water column is nearly constant ($rms(T_{nb}) = 0.008$ °C), being devoid of a tidal signal (Fig. 9).

The vertical structure of $\log_{10} N^2$ for all three stations is shown in Fig. 11. At the upper levels, the variations of stratification are mainly driven by the diurnal heating/

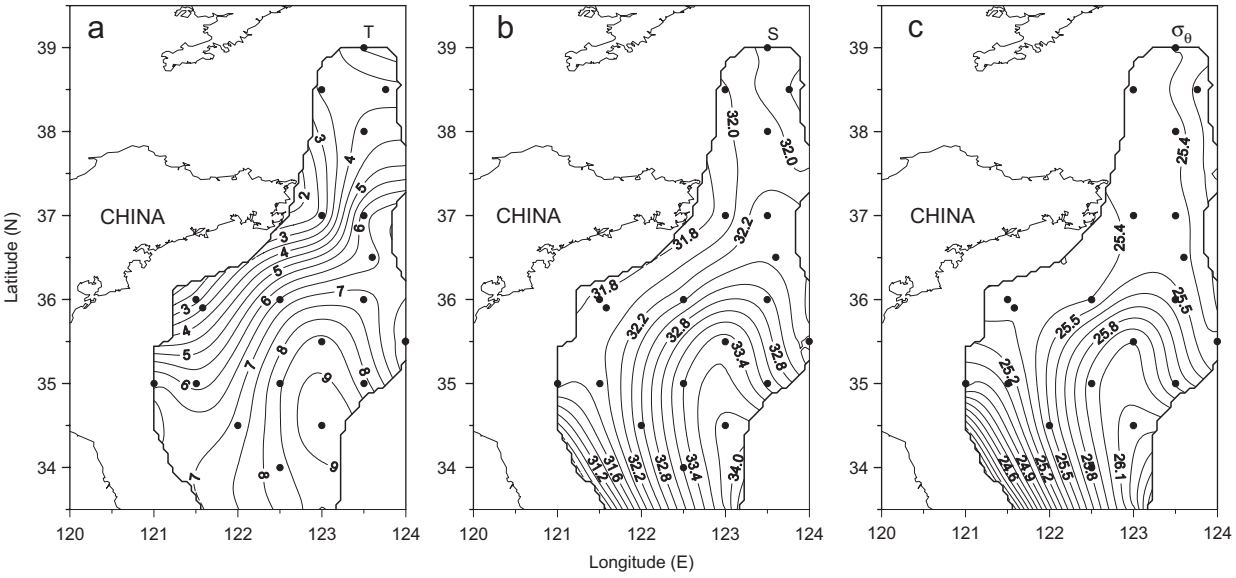

Fig. 8. Temperature (a), salinity (b), and specific density (c) in the northwestern part of the ECS in late March of 2005 ($z = 30$ m).

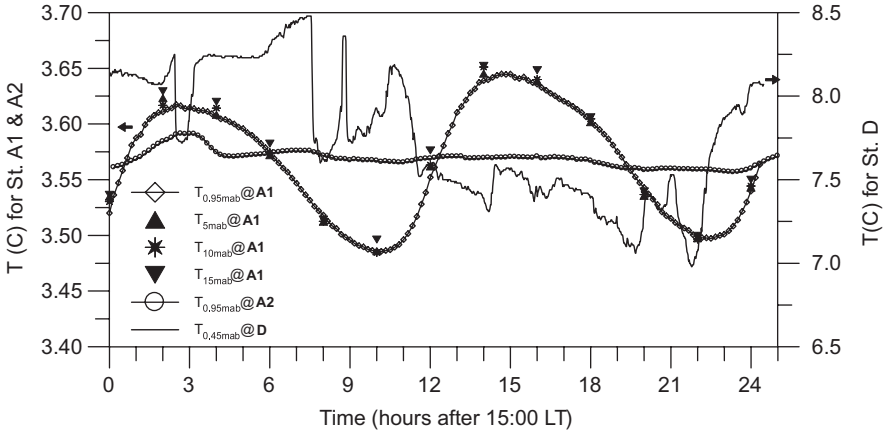

Fig. 9. The near-bottom ($\zeta = 0.95$ and 0.45 mab) ADV measured temperature at the testing sites (left axis is for Sts. A1 & A2, right axis-for St. D.). For A1, the CTD temperatures at $\zeta = 5$, 10, and 15 mab are also shown.

cooling cycle, which is particularly clear at St. A1 (Figs. 10(a) and 11(a)). The discussion henceforth, however, is limited to the near-bottom dynamics, which is the focus of our study. The lower 20 m at Sts. A1 & A2 are weakly stratified, showing $\log_{10} N^2 < -5.1$ (s^{-2}).

At St. D, which is much shallower than A1 and A2, the temperature was nearly constant across the whole water column due to wind mixing at the sea surface and tidal mixing originated near the seafloor. A substantial horizontal temperature gradient between JB waters and the open sea, however, leads to the development of a columnar temporal structure (see Fig. 10(c)) under the influence of reversing tidal flow and higher-frequency seiching. The temperature ranged horizontally (in time) from 7.1 to 8.1 °C. When the u component of the flow reverses its sign, rapid changes in temperature (from ~8.0 to 7.5 °C) occur over a period of less than half an hour (between 11 and 12 LT in Fig. 10(c)).

The water density is not as homogeneous in the vertical as the temperature due to the influence of higher and lower salinity lenses, but the variation of $\log_{10} N^2$ is predominantly temporal/horizontal (see Fig. 11(c)). Because several CTD casts at St. D did not reach the near-bottom layer, a full assessment of near bottom stratification is not possible. The irregular variations of near-bottom temperature at St. D (Fig. 9) over a wide range (7.5–8.5 °C) concurrent with the upper layer suggest that the whole water column was well mixed. This is not surprising considering that at the time of measurements the air temperature was 6–12 °C below the sea surface temperature, ensuring strong convective mixing.

The analysis of stratification at the testing sites indicates that any significant internal wave signatures should not be expected at St. D due to almost completely mixed water column. At Sts. A1 and A2, however, internal waves may exist not only within the near-surface pycnocline, but also

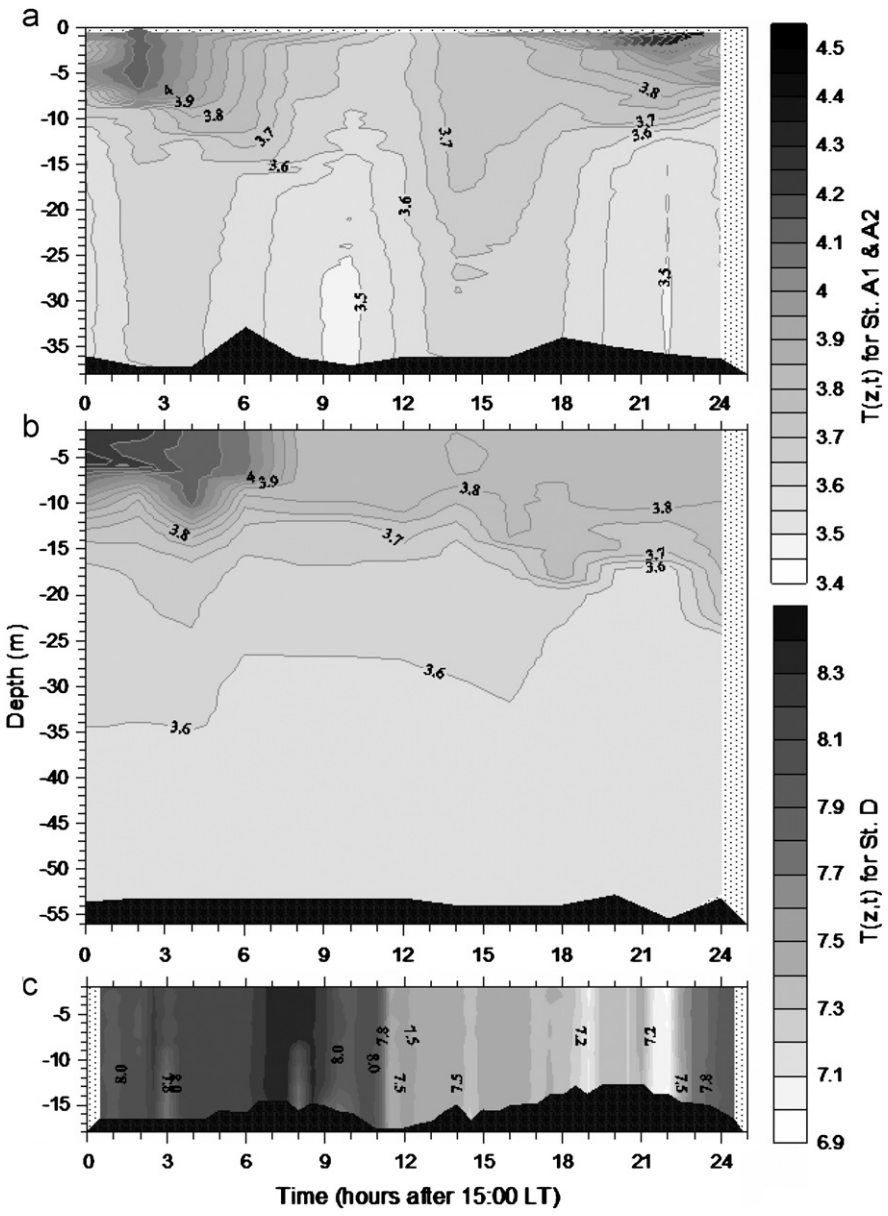

Fig. 10. Temperature contour plots at Sts. A1 (a), A2 (b), and D (c). The blanked depth ranges between the seafloor and the lowest point of CTD profiles are shown at the bottom of each panel (the same in Figs. 11 and 12). Temperature scales are given separately for Sts. A1, A2 and D. The vertical scale for all panels is the same.

in a weakly stratified layer between the pycnocline and the seabed. Because we mostly focus on near-bottom processes, only the lower layer will be of interest ($z >$ 17–20 m at A1, where the mean buoyancy frequency was relatively constant $\bar{N}^2 = (4-6)\times 10^{-6}\,\mathrm{s}^{-2}$). The indication of internal-wave activity can be obtained using the time records of ADCP vertical velocity $w(t)$ at various distances from the seafloor. Fig. 12 exemplifies three characteristic series of $w(t)$: (a)—relatively close to the bottom at $\zeta = 3.9$ mab, (b)—in the middle of weakly stratified layer at $\zeta = 11.4$ mab, and (c)—near the upper boundary of this layer at $\zeta = 18.8$ mab (respective depths are $z = 34.6$, 27.1, and 19.6 m; the vertical step is 10 ADCP cells, equal 7.5 m). The low-frequency trends $\tilde{w}(t)$ in Fig. 12 point to irregular oscillations with approximate M_4 period. The *rms* amplitude of these oscillations in Fig. 12(a) is 0.21 cm/s, decreasing to less that 0.1 cm/s in Fig. 12(b) and increasing again to ~0.13 cm/s in Fig. 12(c). An additional record of $\tilde{w}(t)$ given in Fig. 12(a) for the lowest level of ADCP measurements, $\zeta = 2.4$ mab, indicates a decrease of the amplitude of low-frequency oscillations toward the bottom ($rms(\tilde{w}) = 0.15$ cm/s). The variation of $rms(\tilde{w})$ with the distance from the seafloor indicates possible influence of higher modes of internal tide in shaping the vertical structure of $\tilde{w}$ below the pycnocline. Indeed, integration of the equation for linear internal waves (Turner, 1979) with a characteristic N^2 profile at St. A1 and $w = 0$ at the boundaries, gives, as expected, the maximum of the first

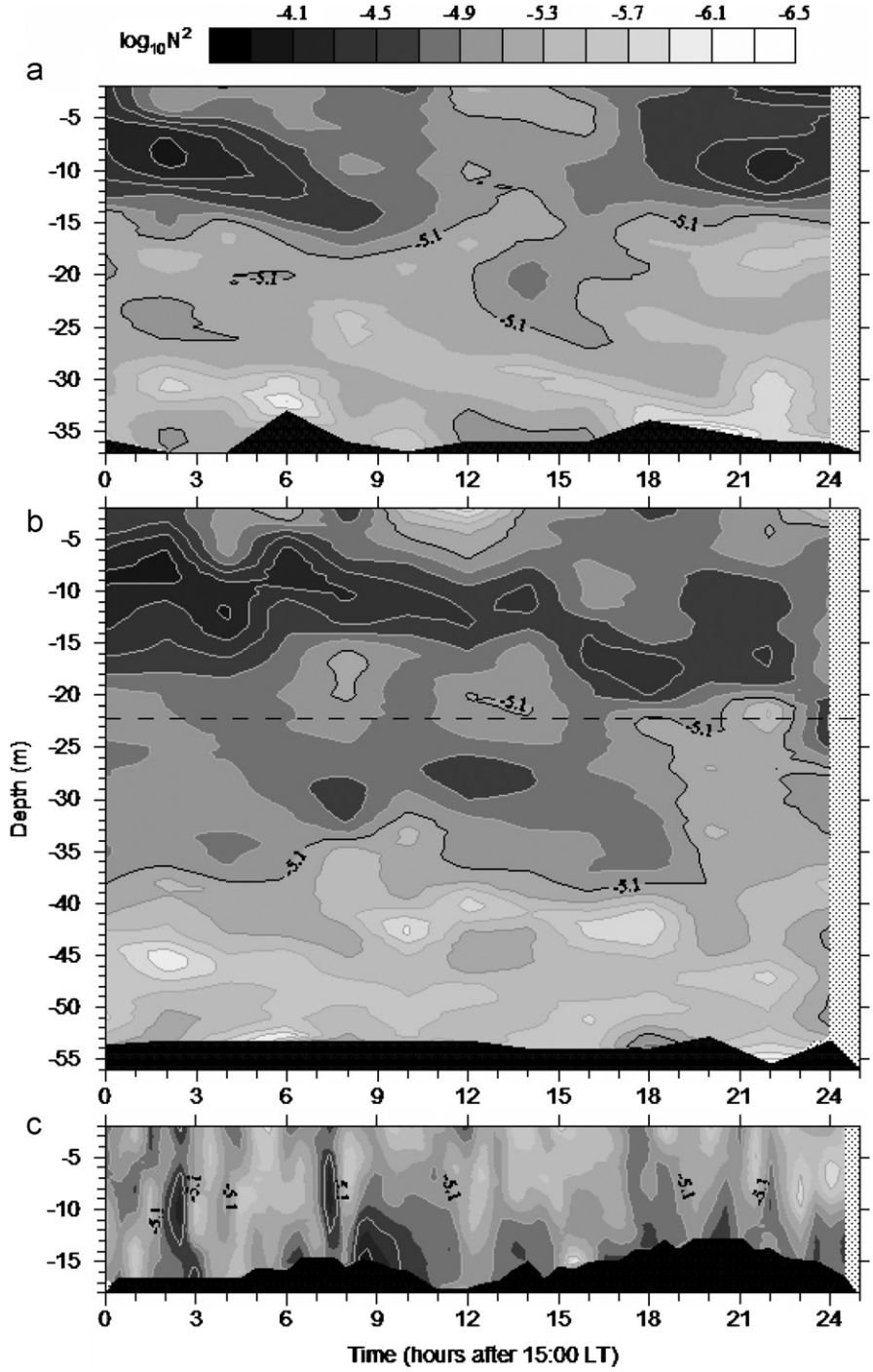

Fig. 11. Contour plots of $\log_{10} N^2$ at Sts. A1 (a), A2 (b), and D (c). Note, a lack of "fine-scale" details at panels (a) and (b) is due to the sparse CTD coverage (every 2 h compared to 0.5 h at St. D). A dashed line in (b) indicates the upper boundary of ADCP data available at St. A2.

mode in the pycnocline at $z = 11$ m. Below the pycnocline, the largest amplitudes of the fourth linear mode were at $z = 18$ and 29 m ($\zeta \sim 20$ and 9 mab) and a zero-crossing at 24 m ($\sim$14 mab). For the fifth mode, the corresponding points are shifted downward for about 2 m. Therefore, the increase of $\tilde{w}$ amplitude upwards from the seabed to $\zeta = 3.9$ mab with the following decrease and increase at $\zeta = 11.4$ and 18.8 mab, respectively, support the notion that the vertical structure of $\tilde{w}(z)$ between the pycnocline and seabed was governed by the fourth and fifth modes of internal tide. Note that the absolute values of low-frequency trends of vertical velocities with periods close to M_2 and M_4 should be taken with caution because even a small pitch/roll of the ADCP position can contaminate values of vertical velocity. Relative values between the trends at various ζ should not be affected by the

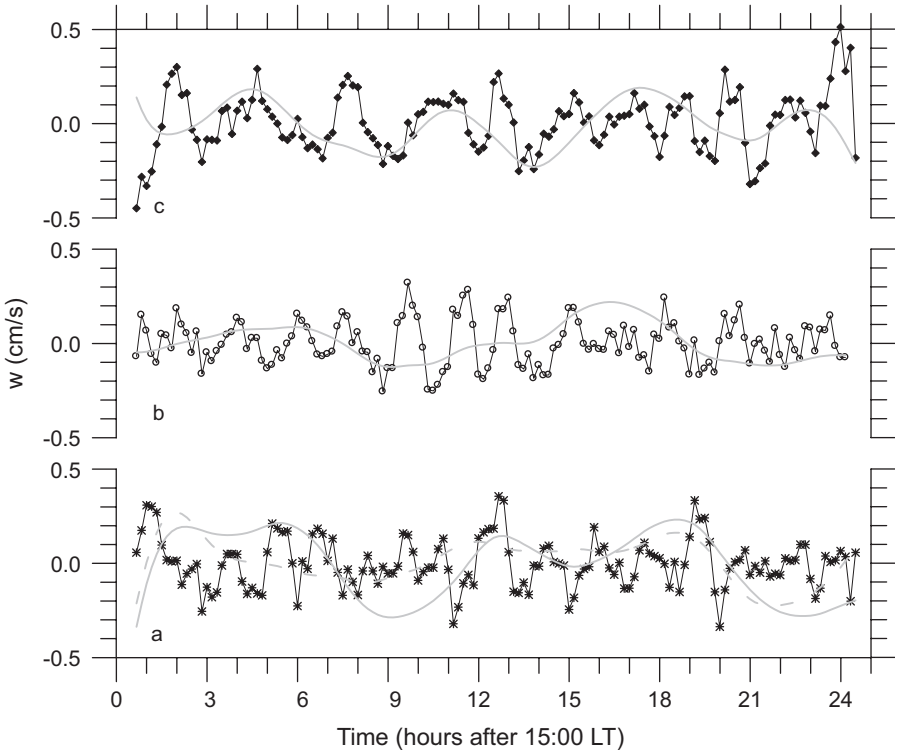

Fig. 12. Examples of the vertical velocity records in the lower part of the water column at St. A1 at $\zeta = 3.9$ (a), 11.4 (b), and 18.9 (c) mab (respective depths $z = 34.6$, 27.1, and 19.6 m) showing short-period internal waves in the background of low-frequency, tidal-affected trends $\tilde{w}(t)$—the heavier continuous lines. The dashed line in (a) is a low-frequency trend close to the bottom at $\zeta = 2.4$ mab.

pitch-related possible contribution to the $\tilde{w}$ magnitude. The filtered, higher-frequency records of $w(z,t)$, which are given in Fig. 12, are not influenced by barotropic tide.

The energy of the semidiurnal internal tide at St. A1 may propagate upslope (Eriksen, 1982; Thorpe, 1987) because the angle of the energy beam $s_{TIW} = \sqrt{(\omega_{td}^2 - F_C^2)/(\overline{N}^2 - \omega_{td}^2)} = 0.023 - 0.035$ is more than twice of the local bottom slope α_b around St. A1. Note $s_{TIW} > 2\alpha_b$ justifies the integration of internal wave equation with the assumption of a flat bottom (Wunsch, 1969). The Coriolis parameter $F_c = 0.77 \times 10^{-4}\,\mathrm{s}^{-1}$ and the mean buoyancy frequency below the pycnocline $\overline{N} = (2 - 2.4) \times 10^{-3}\,\mathrm{s}^{-1}$ were used to estimate s_{TIW}. To the northeast of St. A1, at the tip of Shangdong Peninsula, the bottom slope becomes critical, $\alpha_b = s_{TIW}$, and therefore the energy of internal tide there can be trapped near the seafloor (Thorpe, 1987), generating near-bottom turbulence in addition to the turbulence produced by the friction velocity of barotropic flow. Advection of this additional turbulent kinetic energy along the shelf to the testing site may cause periodic enhancement of kinetic energy dissipation rate observed at St. A1 when the rotated tidal vector was directed from the NE to the SW (between 2-3 and 14–15 LT in Fig. 4). This is discussed in more detail in Lozovatsky et al. (2007).

The records of $w(z,t)$ given in Fig. 12 exhibit quasi-sinusoidal oscillations that can be attributed to higher-frequency internal waves. The spectral densities $E_w(f)$ calculated for these records (see Fig. 13) contain a confident spectral maximum at $f_{w1} = 1.125$ cph ($\tau_{w1} \sim 50$ min) that can be identified in all spectra in the weakly stratified layer below the pycnocline. The frequency of these waves is close to the mean buoyancy frequency

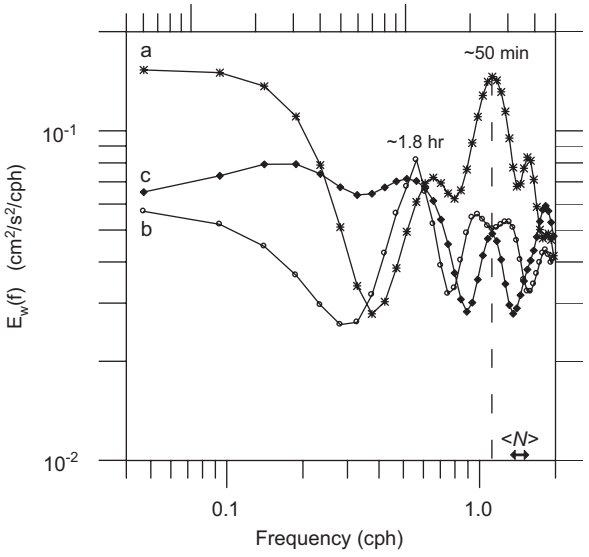

Fig. 13. St. A1: spectral densities of vertical velocity at $\zeta = 3.9$ (a), 11.5 (b), and 18.9 (c) mab (see records in Fig. 12). The range of mean buoyancy frequency in the layer $\langle N \rangle$ is shown along the frequency axis. Two prominent spectral maxima are specified.

$\langle N \rangle \equiv \overline{N} = (2-2.4) \times 10^{-3}\,s^{-1}$ of the layer, which is marked in Fig. 13. The mid-layer spectrum (c) also has a confident maximum at $f_{w2} = f_{w1}/2 = 0.563$ cph ($\tau_{w2} \sim 1.8$ h), which indicates an approximate lower harmonic of the intrinsic frequency internal waves at the site. The deep spectral minima that separate higher-frequency maxima from the low-frequency energetic fluctuations in (a) and (b) spectra in Fig. 13 point to local sources of internal-wave energy. Interaction of tidal flow with irregularities of local bathymetry can excite internal waves of about intrinsic frequency in the lower part of the water column. This assumption is in line with the levels of internal wave spectra (a)–(c). The closest to the seabed spectrum (a) has the highest level of spectral energy peaks compared to spectra (b) and (c) inside the water column below the pycnocline.

6. Velocity profiles and the shear structure

6.1. Velocity profiles

Vertical profiles of horizontal velocity $U(\zeta, t)$ at all testing sites contained a distinct logarithmic boundary layer, which is exemplified in Fig. 14 for a 2-h segment at St. A1. The log layer was easily recognized at Sts. A1 and A2 almost all the time but specifically when the magnitude of tidal vector increased. The estimates of friction velocity obtained by the log-layer approximation of the velocity profiles are discussed in Lozovatsky et al. (2007).

At St. A2, the height of the log-layer H_l varied in a narrow range between 4 and 5 m, increasing to 6–7 m only during a short period of the highest $U(\zeta)$. When $U(\zeta)$ at A2 reached its lowest values at $t = 9$–10 and 15 h (see Fig. 5(a)), which are lower than 0.05 m/s at all heights, the velocity profile temporarily shows a slight decrease of $U(\zeta)$ from the near-bottom level up to the sea surface. Such unusual structure of $U(\zeta)$ has been reported by Guo and Yanagi (1998) during numerical experiments with a three-dimensional model of tidal currents in ECS and YS. The authors argued that the "inverse" vertical structure of $U(\zeta)$ is linked to a particular phase shift between the Coriolis acceleration and the pressure gradient that makes their difference negligible in the water interior. Near the seafloor, however, this difference in combination with a weak vertical stress remains an important driving force that sustains tidal current near the bottom. This suggests that phase variations between the main components of the momentum balance of barotropic tidal flow may cause specific deviations of velocity profile from its traditional increase of U with ζ.

At St. D, the range of the log-layer height H_l was almost the same as at St. A2 (4–5 mab), but the layer was not as apparent as at A1 and A2. Analyzing 176 segments of ADCP data at St. D (512 samples at each segment of 8.5 min long), we found that the log-layer approximation is applicable to 126 segments, most of them belonging to the periods of constant inflow/outflow to/from JB, which accounts for about 70% of the total time of measurements. When the tidal flow was affected by seiching, velocity profiles in the BBL exhibited an increase of U towards the seafloor, showing some similarity with the discussed "inverse" $U(\zeta)$ profiles at St. A2.

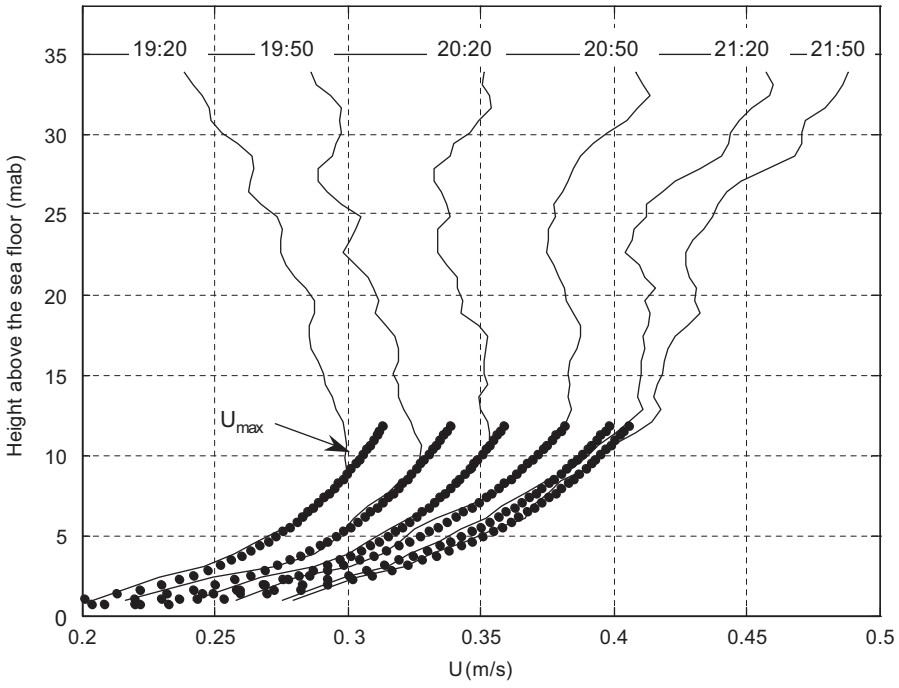

Fig. 14. A series of the run-averaged (3 points) velocity profiles $U(\zeta)$ at St. A1. A distinct maximum U_{max} in the first two profiles ($t = 19{:}20$ and 19:50) gradually disappears with the increase of $U(\zeta)$ to its highest magnitude. The log-layer approximations are shown by the dotted lines between $\zeta = 0.95$ and $\zeta = 12$ mab. (a) Evolution of the velocity profile at St. A1 (the animation can be seen in the electronic version of the paper http://ees.elsevier.com/csr/).

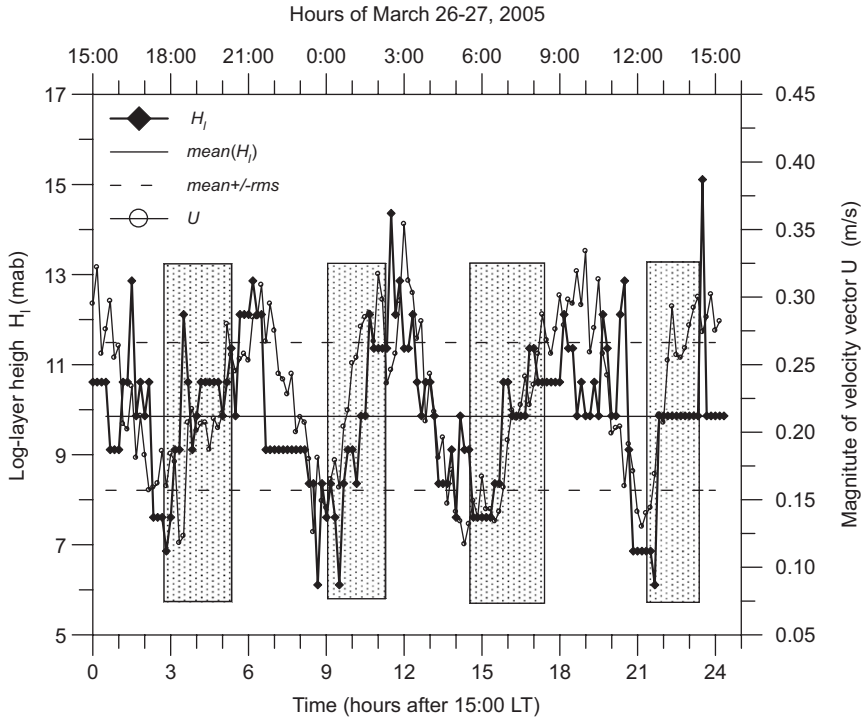

Fig. 15. The variation of the upper boundary of the logarithmic layer H_l (fitted to the velocity profiles) at St. A1 in comparison to the magnitude of the ADV velocity vector U. The shaded segment indicate the periods when $U(\zeta)$ profiles contain a velocity maximum at the upper boundary of the logarithmic layer.

In contrast to Sts. A2 and D, the height of the logarithmic layer at St. A1 varied substantially in time ranging between 6.1 and 15.1 mab. Fig. 15 shows the log-layer height H_l, which was evaluated subjectively as the point where the ADCP velocity magnitude starts to depart from a straight line at the $U(\log(\zeta))$ plots. Variations of H_l follow the M_4 cycle, being closely correlated with $U_{0.95}$ (the correlation coefficient is 0.87). The mean value $\langle H_l \rangle = 9.85$ mab, and the standard deviation $rms(H_l) = 1.62$ mab.

Above the logarithmic layer, the horizontal velocity profiles $U(\zeta)$ at St. A1 typically revealed a distinct maximum U_{max} (see Fig. 14), which exists during the growing phase of barotropic tide. The shaded segments in Fig. 15 mark the periods where U_{max} was observed. The maximum appears first when the current vector is turning from the minor to the major axis of the tidal ellipse; in other words when the magnitude of $U(\zeta)$ starts to increase. The largest amplitude of U_{max} is achieved at the times of the highest acceleration of the flow—at $(dU/dt)_{max}$. Then U_{max} gradually disappears with an increase of $U(\zeta)$ and the velocity profile approaches its usual structure at large $U(\zeta)$ with a permanent increase of barotropic tidal velocity from the seafloor to the surface. In the decreasing phase, the mean velocity gradient above the log layer decreases until $U(\zeta)$ becomes almost homogeneous when the current vector reaches the minor axis of the tidal ellipse. [The evolution of the velocity profile can be seen in the animated Fig. 14(a) of the electronic version of the paper (http://ees.elsevier.com/csr/)].

The increase of tidal velocity initially near the seafloor and only later at the upper levels causes the appearance of U_{max} in the first half of the growing phase of rotating tidal vector. Thereafter, the flow at the upper levels catches up with the near bottom flow and U_{max} disappears. When the tidal vector rotates from the major to the minor tidal axis, the velocity near the sea surface decreases faster than near the bottom, reducing the mean vertical velocity gradient of the profile, but following the general increase of U with ζ until the tidal vector reaches the minor axis.

Several mechanisms can be attributed to the appearance of the velocity maximum above the seabed. In non-oscillating currents, the near-bottom "jet" can be generated due to the decrease of turbulence in sediment-affected flows, perhaps as in the case of "dust storms" (Barenblatt and Golitsyn, 1974). The simple Stokes' solution for oscillatory flow with constant eddy viscosity K_M gives a velocity profile with a maximum above flat bottom at a height H_l, the later being dependent on K_M (Schlichting, 1962). A frontal jet generated at the tidal front due to conservation of potential vorticity between well-mixed and stratified waters (Simpson and Hunter, 1974) may show a local maximum in velocity profiles when the front crosses an observational point (usually it happens in summertime or under the influence of fresh water inflow). In channeled tidal flows (rivers and estuaries), U_{max} appears between ebb and flood transitions (or vise versa) when the near-bottom layer is already occupied by the flood current while the free-surface layer is still affected by the oppositely directed

ebb current. Wind-induced surface currents that are out of phase with tidal currents can also produce a velocity maximum at intermediate depths. The interactions of a tidal flow with internal waves of various frequencies or inertial oscillations related to the rotation of tidal vector are among other possible mechanisms that may manifest U_{max}. In our case, U_{max} is clearly linked to the tidal cycle, thus on the following we discuss only tide-related mechanisms of its origin.

During the first 9 h of observations at St. A1, a drift current affected the upper 10–12 m of the water column, thus reducing the tidal velocity in this layer specifically when the tidal current was directed from the northeastern sector of the shelf (see Fig. 4(a), first 3 h). This happened because the SSE (160–170°) wind of about 6–7 m/s (Fig. 3) induced a surface Ekman current directed from the SSW to the NNE oppositely to the tidal flow. During the next tidal cycle, the wind ceased to ~2 m/s and its influence on the velocity profile diminished even near the sea surface. The interaction between oppositely directed tidal and drift currents created a sub-surface maximum in velocity profiles at a depth of ~8–12 m during first 3 h of observations, but this interaction did not affect the origin of U_{max} above the log layer.

At St. A1, the Simpson and Hunter (1974) parameter $SH = \log_{10}(H_b/\tilde{U}^3) = 2.95$ substantially exceeds the critical values of 1.8–2, that is regarded for the existence of a tidal front (here, the bottom depth $H_b = 38$ m and $\tilde{U} = 0.35$ m/s averaged over the tidal cycle). Wei et al. (2003) mapped the SH parameter over the whole Yellow Sea, showing that in the northwestern sector of the sea (the area of our measurements) the critical SH are concentrated in a narrow shallow zone near the coast. Therefore, the velocity maximum U_{max} cannot be attributed to a tidal frontal jet.

Numerical experiments of Guo and Yanagi (1998) have shown that a local velocity maximum can emerge in the lower part of the water column in homogeneous tidal flow, if the vertical eddy viscosity K_M is depth independent. Vertical profiles with distinct velocity maxima at intermediate depths above the tidally induced BBL have also been recently presented in a series of numerical experiment of Sakamoto and Akitomo (2006), wherein rotating tidal flow and constant eddy coefficients were employed. It is not possible to verify whether K_M is a constant without direct measurements of turbulence inside the water column, but K_M~constant seems to be a reasonable assumption above the log layer for weak stratification observed at the testing site in early spring.

Thus, we may try to model the maximum in velocity profiles $U(\zeta)$ at St. A1 as a sum of the log layer

$$U(\zeta) = (u_*/\kappa)\log(\zeta/\zeta_o), \quad \zeta < H_l, \tag{1a}$$

and an oscillatory tidal flow at its upper boundary (Schlichting, 1962),

$$U(\zeta, t) = \Re\{U_A[1 - \exp(-1+i)\zeta/\sqrt{2K_M/\omega_{td}}]e^{i\omega t}\}, \tag{1b}$$

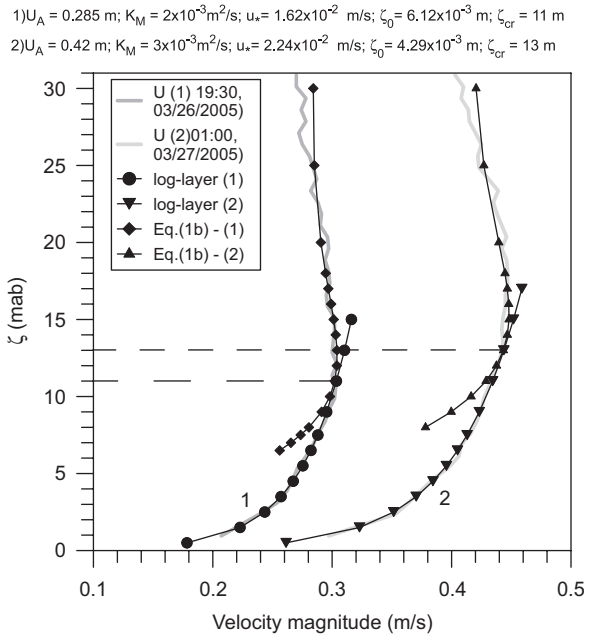

Fig. 16. An example of characteristic velocity profiles (St. A1) with a maximum above the logarithmic layer. The profiles are fitted by a combined log-layer/oscillatory-flow model (Eqs. (1a) and (1b). The boundary ζ_{cr} between two branches of the model is shown by dashed lines.

where U_A is a characteristic amplitude of tidal oscillations. The appropriateness of the approximation (1a,b) is presented in Fig. 16, which shows two characteristic $U(\zeta)$ profiles obtained at $t = 4.5$ and 11 h. To match Eq. (1b) with the observations above H_l, the eddy viscosity should be $(2-3)\times10^{-3}$ m^2/s, which seems to be a reasonable value in weakly stratified waters at the site. Calculations of the eddy diffusivity K_z averaged in the depth range between the pycnocline and the seafloor produced $K_z \sim 2\times10^{-3} - 3\times10^{-4}$ m^2/s (Lozovatsky et al., 2007), which is consistent with the above estimates of K_M. Note that eddy diffusivity K_z is usually smaller than eddy viscosity K_M specifically in stratified flows (e.g., Monin and Yaglom, 1971; Lozovatsky et al., 2006). Sakamoto and Akitomo (2006), for example, ran their numerical experiments with $K_z = 5\times10^{-4}$ m^2/s and $K_M = 5\times10^{-3}$ m^2/s, which were considered by these authors as relatively high values.

A simple model (1a,b) might be applicable only at short time segments because H_l (and therefore the position of U_{max}) would not change with constant K_M, while Fig. 15 clearly shows the variations of H_l approximately with M_4 period. Therefore, as step forward, we allowed K_M to vary in time with the tidal frequency according to

$$K_M(t) = K_{Mo}[1 - \kappa\cos(\omega_{td}t)], \tag{2}$$

where $K_{Mo} = 3\times10^{-3}$ m^2/s is a characteristic eddy viscosity obtained via fitting (1b) to several velocity profiles. We calculated $U(\zeta,t)$ using (1b) with (2) instead of constant K_M. The result is shown in Fig. 17(a) and the variations of vertical shear are given in Fig. 17(b). The contour plot of modeling horizontal velocity resembles tidal current at

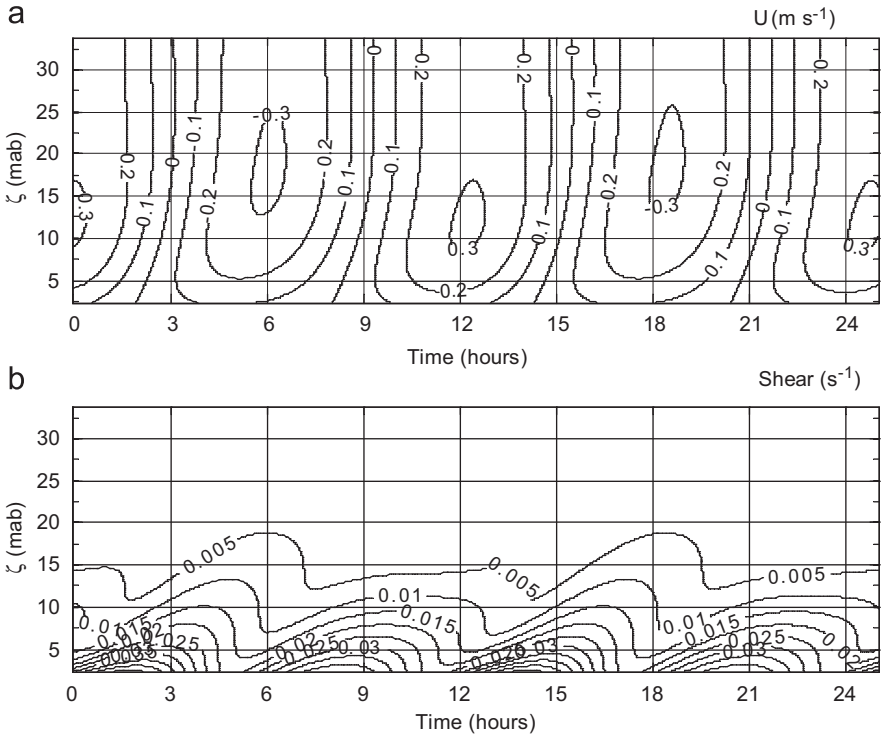

Fig. 17. The contour plot of modeled (based on Eq. (1b) and (2)) horizontal velocity at St. A1 (a) and its vertical shear (b).

St. A1, with a velocity maximum that was observed in $U(\zeta)$ profiles in the depth range 6–15 mab (the modeling maximum is shifted ~5 m upwards, however, which is due to the assigned value of K_{Mo}). Periodic vertical displacements of U_{max} can, therefore, be related to tidal-induced alterations of eddy viscosity at the upper boundary of the log layer. Why this happened at St. A1, but did not at Sts. A2 and D, is not clear yet. As has been mentioned above, the main difference in tidal dynamics between A1 and the other two stations is a steady rotation of the tidal vector at A1 compared to the reversing tide flow at D and mixed, irregular rotation of the tidal current at A2. The rotation itself was not, however, included in Eqs. (1b) and (2) that produced a model structure of tidal flow, which resembles the observed structure of $U(\zeta,t)$ at St. A1. Thus, the rotation of tidal vector can play role in the development of U_{max} and its vertical displacements, but this role is not evident. The alterations of K_M might also be caused by internal waves observed at St. A1 (Fig. 12), which, in turn, could have been generated in response to the rotation of the tidal vector at the site. Verification of this hypothesis requires detailed coupled measurements of velocity and density structure during a longer period.

6.2. Vertical shear

The vertical shear $Sh = \sqrt{(\partial\bar{u}/\partial z)^2 + (\partial\bar{v}/\partial z)^2}$ at all three moorings was calculated using smoothed components of ADCP velocity $\bar{u}$ and $\bar{v}$ after applying the 2nd order Butterworth low-pass filter with a cut-off wavenumber $k_{lp} = 0.13$ cpm ($k_{lp} = 0.2k_N$, $k_N = 1/2\Delta z$, $\Delta z = 0.75$ m). As expected, the largest shear was observed near the seafloor (see Fig. 18), when the M_2 tidal flows reached the highest amplitudes, and near the sea surface due to wind stress. This is most evident at Sts. A1 and D, and to a lesser extent at A2 where the shear was comparatively weaker. High-shear, near-bottom zones, $Sh > (5-7) \times 10^{-3}\,s^{-1}$, extended from the seafloor to the water interior, up to 12–15 mab at A1 (32–40% of the total depth), 7–8 mab at A2 (12–14%), and 7–9 mab at D (37–47%). The high shear was observed more than 80% of the time at A1, less than 20% at A2, and about 40% at St. D. At St. A2, a distinct low-shear zone, $Sh < 10^{-3}\,s^{-1}$, coincided with a layer of increased stratification around $\zeta = 25$ mab ($z = 37$ m), (see the lower secondary pycnocline in Fig. 11(b)). Limited range of the ADCP coverage at this station (37 mab) does not allow investigating this issue in details.

At shallow station D, the shear zones penetrated upwards and downwards, respectively, from the bottom and surface boundary layers into the water interior, periodically forming "chimneys" of high shear across the entire water column (t = ~7–10 and ~17–21 in Fig. 18(c)). When the surface wind ceased, the water interior was occupied by a low-shear zone.

The most instructive shear structure was observed at St. A1, where zones of higher and lower shear appeared periodically at all depths below the wind-stirred surface layer following the increase and decrease of the magnitude of rotating M_2 tide (Fig. 18(a)). The picture is even more striking for components of shear $d\bar{u}/dz$ and $d\bar{v}/dz$

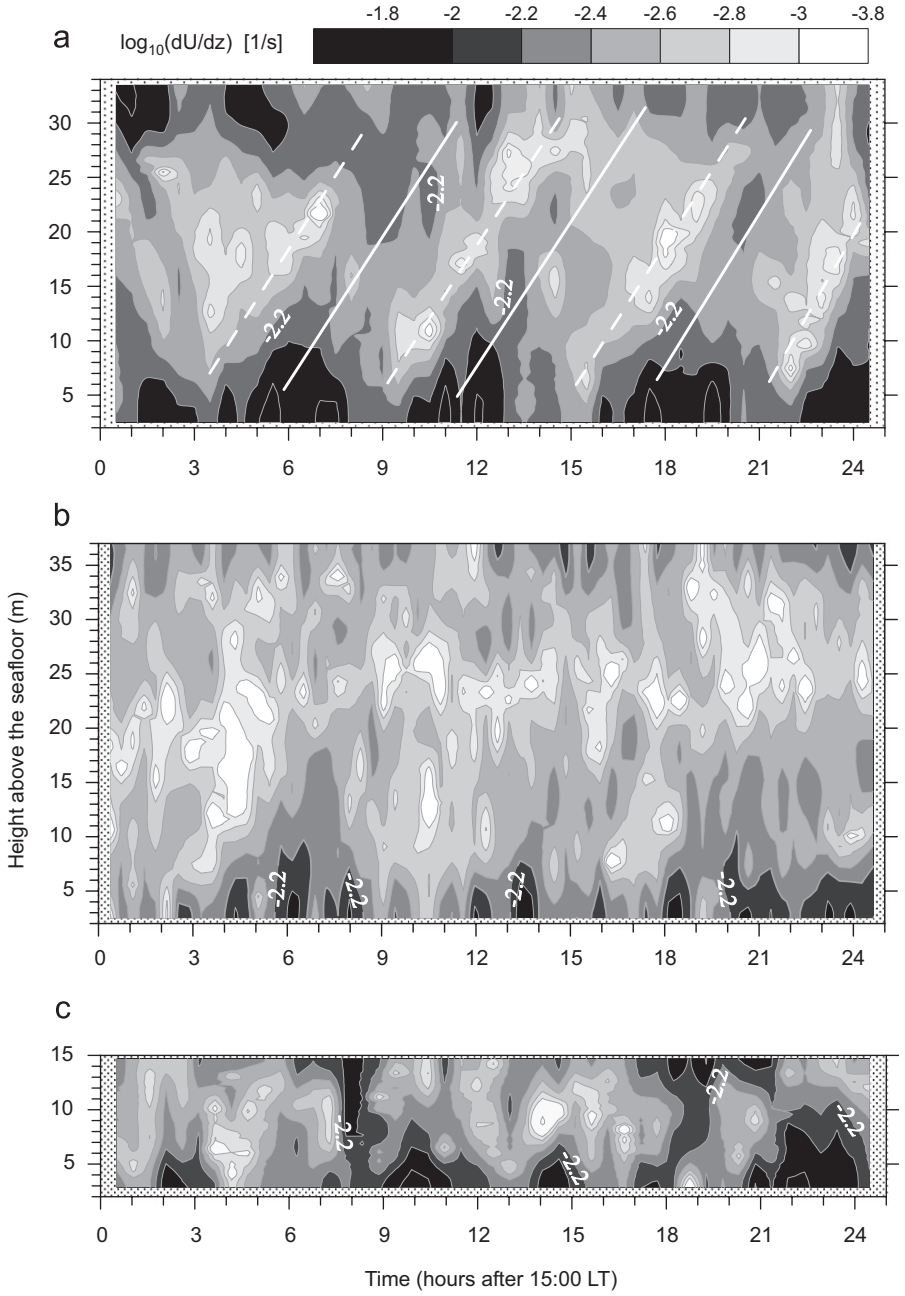

Fig. 18. Contour plots of $\log_{10}(\mathrm{d}U/\mathrm{d}z)$ at Sts. A1 (a), A2 (b), and D (c). High-shear zones are generated near the seafloor at A1 and A2 and propagate to water interior with a phase shift shown in the panels by straight white lines; low-shear bands are marked by dashed black lines. Vertical scales and shaded pallets are identical for all three panels.

(Fig. 19), suggesting that the rotation of tidal vector is a key factor responsible for visual "propagation" of high-shear zones upwards with an approximate "phase speed" of ~5 m/h. The propagation of shear upwards in the lower ~10–15 mab is consistent with the modeled shear structure given in Fig. 17(b) for the eddy viscosity reported in the previous section. The model, however, does not include rotation and the characteristic height of the boundary layer affected by the shear $\delta = \sqrt{2K_M/\omega_T} \sim 7$ m based on $K_M = 3 \times 10^{-3}$ m^2/s. The "propagation" of boundary-generated shear to $\zeta > 10$–15 mab however, would require unrealistically high K_M.

At St. A2 (Fig. 18(b)), the extension of shear zones upward from the bottom is less apparent than at A1. High-shear zones are confined to the lower 20 m of the water column and they "propagate" upwards relatively fast with a phase speed of about 9 m/h for $t < 15$ h. Interestingly, a delay in the time for the appearance of bottom generated shear at a given height at St. A2 can be identified here only during the first 12–15 h of observations, whence the tidal vector made a complete counterclockwise rotation; whereupon the rotation was distorted (see Fig. 5(a)) and the propagation effect was overshadowed. (For $t > 15$ h, the time shift between the

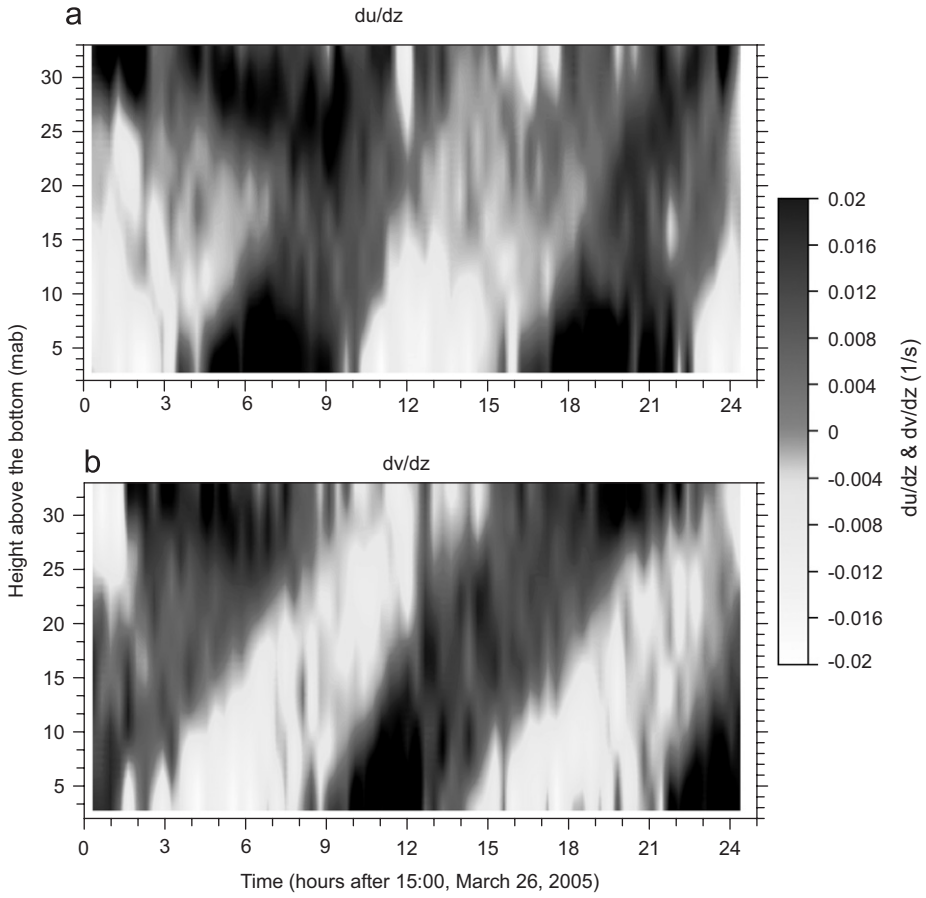

Fig. 19. Contour plots of du/dz (a) and dv/dz (b) at St. A1. The strips of high positive (black) and negative (white) shear zones are produced by the in-phase generation of shear near the bottom and above the log layer. Change of sign of shear at all heights is related to the change of velocity profiles above the BBL. A regular increase of velocity toward the sea surface is followed by a decrease when the current vector rotates from the minor to the major axis of the tidal ellipse.

generation of high shear near the bottom and at the upper levels is almost zero).

It is evident that the observed slow "propagation" of the boundary-generated shear is related to the specifics of velocity profile, which contains a distinct maximum at the upper boundary of the log layer and the upward/downward movement of its location during the tidal cycle. Fig. 17(b) indicates that even a simple version of Stokes' oscillatory BBL model with time-dependent but vertically uniform K_M can yield the observed sloped shear zones in the lower 10–15 mab. The generation of shear above U_{max} relates to a substantial decrease of the tidal magnitude toward the sea surface during the first half of the growing phases of tidal vector (predominantly southward–northward currents). It is interesting that the time evolution of $U(\zeta, t)$ above U_{max} has the same "phase speed" as that of the BBL, ensuring almost constant slope of 5 m/h for the alternating shear zones in Figs. 18(a) and 19. Explanations available for the shape of the velocity profile at St. A1 (Section 6.1), do not, however, elucidate why such identical time lags exist below and above U_{max}. As mentioned, Guo and Yanagi (1998) attributed unusual shapes of velocity profiles (maximum above the BBL, a decrease toward the sea surface) to the differences in the phases of main terms of the momentum balance of rotating tidal flow. A specific combination of local tidal conditions and associated mixing patterns (time-dependent K_M) may favor the development of a local maximum above the BBL or even a decrease of $U(\zeta)$ upwards from the seafloor. When the wind-induced shear is in phase with the tidal shear, the sloping shear zones may occupy the whole water column (Fig. 18(a)).

A related phenomenon of the upward propagation of dissipation ε has been observed in the Irish Sea (Simpson et al., 1996; Rippeth et al., 2003), which has been modeled by Simpson et al. (1996) and Burchard et al. (1998). The dissipation akin to boundary shear production reported in these studies (see also Rippeth, 2005 for general discussion) propagated upwards with a high phase speed ~10–50 m/h. More recent measurements show that the phase shifts may vary with the distance from the seafloor (Simpson et al., 2007). The reduction of K_M due to stable stratification in BBL has been suggested as a possible explanation for slower propagation of the dissipation upwards. This is consistent with the simple tidal BBL model, wherein the rate of "shear propagation" is $c \sim \sqrt{2\omega_T K_M}$. Our data at

St. A1 and A2, where stratification below the thermocline was almost the same but the shear structure quite different, do not fit this explanation well. It is possible that other factors such as the rotation of tidal vector rather than weak stratification can be the reason. Note also that a decrease of mixed layer depth at high latitudes due to suppression of shear-induced turbulence by Coriolis force has been reported in several numerical experiments (e.g., Lozovatsky et al., 2006), and a similar phenomenon is plausible here for the rotating tidal flow.

7. Summary

In this study, we analyzed tidal-driven motions along the Chinese coast of the ECS (the Yellow Sea). Measurements were conducted in three testing sites during March (Sts. A1 and A2) and December (St. D) of 2005 using bottom-mounted ADV and ADCP instruments and CTD profiler. A shallow-depth (19 m) St. D was located near the mouth of the Jiaozhou Bay (JB) about 1 mile from the coastline. St. A1 was set up at the sloping shelf (38 m depth), about 90 km east off the coast, and St. A2 was in a deeper northern basin (56 m depth) near the BS (Fig. 1). Circulation in the region was dominated by the Yellow Sea Coastal Current, which follows southward along the China coast (Fig. 2). At Sts. A1 and A2, the winds were calm or moderate ($\langle W_{10} \rangle = 4.0 \pm 1.8$ m/s at A1 and $\langle W_{10} \rangle = 5.2 \pm 2.6$ m/s at A2). Weak buoyancy flux at the sea surface did not influence the water interior below the pycnocline ($z = 12$–15 m). The lower 20 m of the water column were weakly stratified ($N^2 < 10^{-5}\,\mathrm{s}^{-2}$) as a result of boundary mixing and remnants of winter convection (Figs. 10 and 11). At St. D, strong convection-favorable buoyancy flux, $\sim 1.3 \times 10^{-7}$ W/kg, caused the whole water column to become well mixed.

The testing sites were subjected to substantially different regimes of barotropic tide (Figs. 4–6). A regular, slightly stretched ellipse of counter-clockwise rotating, predominantly semidiurnal, barotropic tide was observed at St. A1. At St. A2, the tidal ellipse was irregular and twisted. The characteristic amplitude of M_2 tidal constituent at A1 and A2 was 0.35 and 0.42 m/s, respectively.

Near the coast at St. D, the tidal flow was reversing and behaving similar to an oscillating flow. The M_2 amplitude of the western flood current was 0.4 m/s, twice that of the eastern ebb current. This zonal tidal flow was superimposed by higher-frequency oscillations with a period $\sim$2.3 h, which could be attributed to seiching generated in JB. Estimates of the seiche frequency (period) were in agreement with the frequencies of spectral maxima of the sea surface elevation and the energy of horizontal components (Fig. 7).

The variations of near-bottom temperature $T_{nb}(t)$ at St. A1 were clearly of tidal origin; at St. D, irregular variations of $T_{nb}(t)$ did not show any tidal signal and at St. A2, T_{nb} was almost constant (Fig. 9). Apparent tidal variations of $T_{nb}(t)$ at St. A1 (see Figs. 9 and 10(a)) were caused by the advection of tidal flow across horizontal temperature gradient at the sloped shelf rather than semidiurnal internal tide in the region. The energy of internal tide at St. A1 may propagate upslope because its beam angle (0.023–0.035) substantially exceeds the local bottom slope.

Relatively short-period internal waves were identified in a weakly stratified layer between the pycnocline and the seafloor (Figs. 12 and 13) with maxima in spectra of vertical velocity $E_w(f)$ at $f_{w1} = 1.125$ cph ($\tau_{w1} \sim 50$ min) and $f_{w2} = f_{w1}/2 = 0.563$ cph ($\tau_{w2} \sim 1.8$ h). The analysis of internal waves at various levels points to a local source of internal-wave energy, which could be related to the interaction of tidal flow with irregularities of local bathymetry that excites internal waves of approximate intrinsic frequency in the lower part of water column.

The height of the logarithmic boundary layer at the sloping shelf (A1) varied with tidal cycle between 6 and 15 m (Figs. 14 and 15). In the deeper northern basin (St. A2) and at shallower St. D, the log-layer extended to $\sim$4–6 mab. A maximum of horizontal velocity U_{max} appears at St. A1 above the log layer when the current vector rotates from the minor to the major axis of the tidal ellipse (during approximately 3 h of this phase, Figs. 14 and 14(a)). The vertical profile of horizontal velocity therein could be represented by a combination of log layer and an oscillatory (Stokes' type) flow with the modeled eddy viscosity for the latter being $K_M = (2-3) \times 10^{-3}\,\mathrm{m}^2/\mathrm{s}$ (Fig. 16). We also modeled velocity and shear structures in the BBL with a time varying but vertically uniform eddy viscosity during M_2 cycle. The modeling result (Fig. 17) shows qualitative agreement with measurements at St. A1. The use of time-dependent K_M formally violates the basic assumption of the Stokes' formula (1b) that was derived for a constant K_M, and hence the results obtained only hint that time-dependent eddy viscosity may be responsible for vertical displacements of U_{max}.

The largest shears at all stations were found near the seafloor, when the M_2 tidal flow reached the highest amplitudes, and near the sea surface due to wind stress (Fig. 18). The rotating tidal flow at St. A1 revealed a slow upward "propagation" of shear generated at the seafloor into the ocean interior up to $\zeta = 10$–15 mab with a phase speed $\sim$5 m/h (Figs. 18(a) and 19). This phase speed estimate was a factor of two smaller than that for irregularly rotating flow at St. A2. For reversing tidal flow at St. D, the shear extends upwards from the seafloor with almost no time delay. Our analysis suggests that a rotating tide may generate substantially different patterns of shear compared to reversing tidal flow, and this disparity has implications in turbulence and mixing in ECS. Further discussion is given in Lozovatsky et al. (2007).

Acknowledgments

The cruises were organized by Ocean University of China in Qingdao. We wish to thank scientists and students of OUC who participated in the measurements and data

collection and the crew of R/V *Dongfanghong*-2. The support to the first and fourth authors was provided by the US Office of Naval Research (Grant N00014-05-1-0245). The second and third authors were supported by the Major State Program of China for Basic Research (Grant no. 2006CB400602), and the National Foundation of China for Natural Science (Grant no. 40490260). We appreciate comments of two anonymous reviewers, which were very helpful.

Appendix A. Supplementary materials

Supplementary data associated with this article can be found in the online version at doi:10.1016/j.csr.2007.08.006.

References

Barenblatt, G.I., Golitsyn, G.S., 1974. Local structure of mature dust storms. Journal of the Atmospheric Sciences 31 (7), 1917–1933.

Burchard, H., Petersen, O., Rippeth, T.P., 1998. Comparing the performance of the Mellor–Yamada and the k–ε two-equation turbulence models. Journal of Geophysical Research 103 (C5), 10,543–10,554.

Eriksen, C.C., 1982. Observations of internal wave reflection off sloping bottoms. Journal of Geophysical Research 87 (C1), 525–538.

Fairbridge, R.W., 1966. In: The Encyclopedia of Oceanography, vol. 1, pp. 994–998.

Fang, G.H., 1974. Quasi-harmonic constituent method for analysis and prediction of tides I: quasi-harmonic constituents. Studia Marina Sinica 9, 1–15 (in Chinese, with English abstract).

Fang, G.H., 1976. Quasi-harmonic constituent method for analysis and prediction of tides II: analysis of short period observations. Studia Marina Sinica 11, 33–55 (in Chinese, with English abstract).

Fang, G.H., 1981. Quasi-harmonic constituent method for analysis and prediction of tides III: a practical procedure for analyzing tidal streams and tidal elevations. Studia Marina Sinica 18, 19–39 (in Chinese, with English abstract).

Guo, X., Yanagi, T., 1998. Three-dimensional structure of tidal current in the East China Sea and the Yellow Sea. Journal of Oceanography 54 (6), 651–668.

Kang, S.K., Foreman, M.G., Lie, H.-J., Lee, J.H., Cherniawsky, J., Yum, K.-D., 2002. Two-layer tidal modeling of the Yellow and East China Seas with application to seasonal variability of the M_2 tide. Journal of Geophysical Research 107, 3020.

Knauss, J.A., 2000. Introduction to Physical Oceanography, second ed. Pearson, Prentice-Hall, New Jersey, 309pp.

Lee, J.C., Jung, K.T., 1999. Application of eddy viscosity closure models for the M_2 tide and tidal currents in the Yellow Sea and East China Sea. Continental Shelf Research 19 (4), 445–475.

Liu, Z., Wei, H., Liu, G., Zhang, J., 2004. Simulation of water exchange in Jiaozhou Bay by average residence time approach. Estuarine, Coastal and Shelf Science 61, 25–35.

Lozovatsky, I., Roget, E., Fernando, H.J.S., Figueroa, M., Shapovalov, S., 2006. Sheared turbulence in a weakly stratified upper ocean. Deep-Sea Research I 53, 387–407.

Lozovatsky, I.D., Liu, Z., Wei, H., Fernando, H.J.S., 2007. Tides and mixing in the northwestern East China Sea. Part II: the near-bottom turbulence. Continental Shelf Research, in press, doi:10.1016/j.csr.2007.08.007.

Monin, A.S., Yaglom, A.M., 1971. Mechanics of Turbulence. In: Statistical Fluid Mechanics, vol. 1. MIT Press, Cambridge, MA, 782pp.

Rippeth, T.P., Simpson, J.H., Williams, E., 2003. Measurement of the rates of production and dissipation of turbulent kinetic energy in an energetic tidal flow: Red Wharf Bay revisited. Journal of Physical Oceanography 33, 1889–1901.

Rippeth, T.P., 2005. Mixing in seasonally stratified shelf seas: a shifting paradigm. Philosophical Transactions of the Royal Society A 363, 2837–2854.

Sakamoto, K., Akitomo, K., 2006. Instabilities of the tidally induced bottom boundary layer in the rotating frame and their mixing effect. Dynamics of Atmospheres and Oceans 41, 191–211.

Schlichting, H., 1962. Boundary Layer Theory, sixth ed. McGraw-Hill, New York, 744pp.

Simpson, J.H., Hunter, J.R., 1974. Fronts in the Irish Sea. Nature 250, 404–406.

Simpson, J.H., Crawford, W.R., Rippeth, T.P., Cambell, A.R., Cheok, J.V.S., 1996. The vertical structure of turbulent dissipation in shelf seas. Journal of Physical Oceanography 26, 1579–1590.

Simpson, J.H., Green, J.A.M., Osborn, T., Nimmo-Smith, T.W.A.M., Rippeth, T.P., 2007. Turbulent dissipation across a tidal mixing front. In: Abstracts of the 39th International Liège Colloquium on Ocean Dynamics and the third Warnemünde Turbulence Days, Turbulence Re-Revisited, 7–11 May 2007, 〈http://modb.oce.ulg.ac.be/colloquium/2007.submit.html〉.

Song, W., 1994. Characteristics of summer and winter circulations and their variability as the source of the Tsushima Warm Current. Acta Ocenologica Sinica 13, 189–201 (in Chinese).

Su, J., 1998. Circulation dynamics of the China seas: north of 18°N. In: Robinson,, A.R.,, Brink,, K., (Eds.), The Sea, vol. 11. The Global Coastal Ocean: Regional Studies and Syntheses. Wiley, New York, pp. 483–506.

Thorpe, S.A., 1987. On the reflection of a train of finite-amplitude internal waves from a uniform slope. Journal of Fluid Mechanics 178, 279–302.

Turner, J.C., 1979. Buoyancy Effects in Fluids. Cambridge University Press, Cambridge, 368pp.

Wei, H., Su, J., Wan, R., Wang, L., Lin, Y., 2003. Tidal front and the convergence of anchovy (Engraulis japonicus) eggs in the Yellow Sea. Fisheries Oceanography 12 (4/5), 434–442.

Wunsch, C., 1969. Progressive internal waves on slopes. Journal of Fluid Mechanics 35, 131–144.

Yuan, Y., Su, J., 1984. Numerical modeling of the circulation in the East China Sea. In: Ichiye, T. (Ed.), Ocean Hydrodynamics of the Japan and East China Seas. In: Elsevier Oceanographic Series, vol. 39. Elsevier, New York, pp. 167–186.